Phonon Dynamics of Exotic Materials Bi_2Se_3, Bi_2Te_3, Sb_2Te_3 and WSe_2

by

©Kolawole Akintola

B. Sc. (2008) Obafemi Awolowo University, Nigeria

A thesis submitted in partial fulfilment of

the requirements for the degree of

Master of Science (Physics)

Department of Physics and Physical Oceanography

Memorial University of Newfoundland

October 2014

St. John's Newfoundland

Abstract

Raman and Brillouin spectroscopy have been employed to investigate the phonon dynamics of Bi_2Se_3, Bi_2Te_3, Sb_2Te_3 (all topological insulators) and WSe_2 (a 2D semiconductor). In the frequency range studied, two peaks were observed in the Raman spectra of Bi_2Se_3, Bi_2Te_3, Sb_2Te_3. Polarization studies were done to study the nature of these peaks and assign them to particular vibrational modes. Due to the fact that all three materials belong to the same space group and have the same Wyckoff positions, it stands to reason that their Raman spectra will be identical in every respect except for the position where the peaks appear. This was found only to be partially true from what we observed. The presence of Te atoms in Bi_2Te_3, and Sb_2Te_3 was observed to play a prominent role in determining mode intensity. We verified that the higher intensity of the peak observed due to the $A_{1g}^{(2)}$ mode compared to that due to the $E_g^{(2)}$ mode in Bi_2Te_3, and Sb_2Te_3, is most probably due some resonance effect induced by the laser excitation wavelength used.

Raman scattering studies of WSe_2 have generated much controversy with regards mode assignment and the shifts at with spectral peaks appear while there are no reports from Brillouin scattering studies of this material. Our Raman experiment shows that the Raman active $E_{2g}^{(1)}$ and A_{1g} modes in WSe_2 initially thought to be degenerate are not degenerate. This was verified by collecting spectra at different polarization configurations. One of the polarization configurations showed two closely separated peaks, enabling us to identify the constituent modes from the originally near-degenerate mode in the unpolarized spectrum. The velocity of the Rayleigh surface wave was extracted from the Brillouin spectra collected at different angles of

incidence ranging from 35 to 80 degrees in a Brillouin light scattering experiment. The value of the velocity compares well with those previously reported for related materials.

This work reports new results on the vibrational properties of Bi_2Se_3, Bi_2Te_3, Sb_2Te_3 and WSe_2. Our results also resolves the inconsistencies reported in previous studies on the vibrational properties of these materials.

Acknowledgements

I would like to specially thank my supervisors, Dr. Todd Andrews and Dr. Stephanie Curnoe for their unrelenting assistance and guidance throughout the course of my research and program. I would also like to show my gratitude to Dr. Ania Harlick and Dr. M. J. Clouter for their support and advise, to Dr. Erika Merschrod for making her lab available to me for my research and to the entire faculty and staff of the Department of Physics, Memorial University of Newfoundland for standing by me in difficult times.

Finally, I would also like to express my gratitude to my late father, Mr. P. A. Akintola from whom I learned that I can be the best person I want to be. He also taught me to love others as myself and show gratitude to any form of kindness I receive. Also, I will like to thank my Mum, my siblings and friends, without their help and encouragement I would not have gotten this far. I pray the Almighty God bless and replenish them all.

Contents

List of Tables

List of Figures

Chapter 1

Introduction

1.1 Exotic Materials

Research into the physics of materials exhibiting novel characteristics has been generating a lot of momentum over the last few years. Their electronic properties have generated a lot of debate. The phonon dynamics of two such material classes, topological insulators and 2D semiconductors, provide the basis of discussion in this thesis. Information about the vibrational states of these materials are extracted from our experimental observations.

1.1.1 Topological Insulators

The intriguing physical properties displayed by recently discovered materials has defined the face of research in condensed matter physics. In the last decade, the physics community has welcomed the discovery of a number of materials exhibiting characteristics that had not been previously realizable experimentally. Amongst such

exotic materials are topological insulators which were discovered in 2007 [1]. Topological insulators, many of which are already known semiconductors, are materials having a band gap in the bulk but a gapless surface state. In other words, they are insulators in the bulk but conductors on the surface. The discovery of topological insulators was more of the discovery of a novel property in existing materials rather than the discovery of new materials. Topological insulators are typically synthesized in the laboratory, but recently, this property was observed in Kawazulite, a naturally occurring mineral found in gold mines [2]. It got its name from the Kawazu mine in Japan, where it was first discovered. Kawazulite was found to have the following composition $Bi_2(Te,Se)_2(Se,S)$.

As recently as 2005, Kane and Mele [3] proposed that the spin orbit interaction can lead to topological insulating electronic phases. Later, Kane and Mele [4], Liang and Kane [5], Moore and Balents [6], and Roy [7] made the same predictions before this exotic phase was observed in experiments on real materials [1, 5, 8–11]. In ordinary insulators, the conduction and valence bands are well separated by a large energy gap such that the electrons in the filled valence band do not have sufficient energy to be thermally excited into the conduction band. In another class of insulators, the energy gap is modified due to the presence of the spin-orbit interaction (spin and orbital angular momentum coupling of an electron). This leads to a band gap inversion states initially lying above the gap are now lying below, and vice versa. This introduces complexity into the band structure which is evident in the surface state becoming conducting, hence the name topological insulators. In the same vein, topological insulators can be described as materials having an insulating bulk with conducting surface states protected by time reversal symmetry (a transformation that reverses

the arrow of time; T: $t \rightarrow -t$). The presence of time reversal symmetry ensures that the surface states have band crossings and no band gap. On breaking time reversal symmetry (which can be achieved by adding a magnetic field) the crossing bands will mix, thereby opening a gap in the energy spectrum. This means that changes at the surface will not remove the conducting states, *i.e.* there will never be a band gap unless time reversal symmetry is broken, at which point the surface state may become insulating.

Topological insulators have been classified as 2D or 3D depending on their dimension. A 2D topological insulator is analogous to a quantum spin Hall insulator [12], since both share the property of being insulating in the bulk with topologically protected edge states. This state was first proposed to exist in graphene (monolayer graphite). The ground state of graphene exhibits the quantum spin Hall effect with an energy gap due to spin orbit interaction [3]. The quantum spin Hall effect has also been observed in $Hg_{1-x}Cd_xTe$ quantum wells. It is worth mentioning that spin-orbit coupling in $Hg_{1-x}Cd_xTe$ quantum wells is larger due to the heavy elements involved compared to carbon in graphene. The magnitude of the spin-orbit interaction determines the strength of the topological insulator. As a result $Hg_{1-x}Cd_xTe$ quantum wells form a family of stronger 2D topological insulator compared to graphene.

The discovery of a quantum spin Hall insulator (2D topological insulator) gave a template for generalization to 3D. In 3D, the surface states are gapless and protected against perturbations to the Hamiltonian. On introducing perturbations that break the time reversal symmetry of the Hamiltonian or on a closure of the bulk band gap, the system ceases to be a topological insulator. In the simplest case, a 3D topological insulator can be formed by stacking layers of two-dimensional quantum spin Hall

insulators along a particular axis, with the helical edge states of the layers becoming surface states which are not time reversal protected, (unlike the helical edge states themselves). The 3D topological insulator formed in this case has the topological invariant $\nu_0 = 0$ which describes a weak topological insulator. The scenario $\nu_0 = 1$ is a strong topological insulator, which cannot be described by the stacking of quantum spin Hall insulators. A weak topological insulator is one in which a gap can open up on the surface state without necessarily breaking time reversal symmetry while a strong topological insulator requires breaking of time reversal symmetry before a gap can occur. More on the differences between these types of 3D topological insulators can be found in [13].

The surface electronic structure of 3D topological insulators is similar to that of graphene; the only obvious difference is that in graphene there are 4 Dirac points, while 3D topological insulators have a single Dirac cone at k=0 (Γ point) of the Brillouin zone. A Dirac point if formed from the liner relationship between energy $E(k)$ and wave vector k giving rise to Dirac cones. The point where two Dirac cones merge is called the Dirac point. It is a point where the density of state is zero. Charge transport experiments, which were successful for identifying 2D topological insulators, are problematic in 3D materials because the significance in the conductivity of the topological character of the surface states is more subtle in 3D; rather Angle-resolved photoemission spectroscopy experiments are more suitable.

After their existence was predicted in 2005, the first 3D topological insulator was synthesized and observed by experimentalists in 2008 when Hsieh *et al.* [9] found a topological insulating state in $Bi_{1-x}Sb_x$. The small band gap and complex surface state in $Bi_{1-x}Sb_x$ necessitated the need to find topological insulators with larger band

gap and a simpler surface. This led to the discovery of second generation materials: Bi_2Se_3; Bi_2Te_3; and Sb_2Te_3. These three second generation TIs will be studied in this thesis.

Several experimental techniques have been employed in probing the properties of topological insulators. Angle-resolved photoelectric spectroscopy results have shown that the 3D topological insulators Bi_2Se_3, Bi_2Te_3, and Sb_2Te_3 have a single Dirac cone on the surface [11, 14]. Some other properties probed by various techniques are: the nature of the surface states using Scanning Tunnelling Microscope [15, 16]; elastic constants using continuous-wave resonance experiments [17]; vibrational properties of thin films using Raman spectroscopy [18–25]; lattice thermal expansion coefficient using X-ray diffraction [26]. A review of the properties of topological insulators may be found in [12, 27].

Potential applications of bulk topological insulators have been suggested in the fields of super-computing and spintronics due to the fact that they contain surface states that are topological protected against time reversal symmetry, while thin film topological insulators have been proposed to be applicable in magnetic memory where write and read operations are achieved by purely electric means since the presence of a magnetic field will break time reversal symmetry.

1.1.1.1 Bi_2Se_3, Bi_2Te_3, and Sb_2Te_3

The topological insulating property has been observed in bismuth and antimony chalcogenides, particularly in Bi_2Se_3, Bi_2Te_3, and Sb_2Te_3. Before their discovery as topological insulators, they had been deployed as thermoelectric materials for converting thermal power into electrical power and vice versa. Only recently were they

confirmed to be members of a family of second generation 3D topological insulators. A connection between the topological insulating property and the thermoelectric properties of these materials is yet to be observed/reported.

Bi_2Se_3, Bi_2Te_3, and Sb_2Te_3 crystallize in the rhombohedral crystal structure with space group $D^5_{3d}(R\bar{3}m)$ with five atoms in a unit cell [21]. The crystal is formed by stacking five-atom layers along the z direction. Each 5-atom layer is known as a quintuple layer (QL), with a thickness of about 0.96 nm [21]. The atoms within a single QL are held together by strong covalent forces while the force between QLs is much weaker and of the van-der-Waals type. Some of the novel properties in these materials have been attributed to the presence of the van-der-Waals force. Single crystals of Bi_2Se_3, Bi_2Te_3 and Sb_2Te_3 have the following symmetry elements:

- Trigonal axis (3 fold rotation symmetry) defined as the $z-$axis
- Binary axis (2 fold rotation symmetry) defined as $x-$axis
- Bisectric axis (in the reflection plane) defined as $y-$axis
- Inversion centre.

The arrangement of atoms takes the same form in all three materials. In Bi_2Te_3 form instance, the atoms are arranged in the form $Te^{(1)}-Bi-Te^{(2)}-Bi-Te^{(1)}$ where the superscript on the Te atoms represents different positions within a quintuple layer, consequently positions (1) and (2) are not equivalent. Figure 1.1 shows this arrangement for Bi_2Te_3.

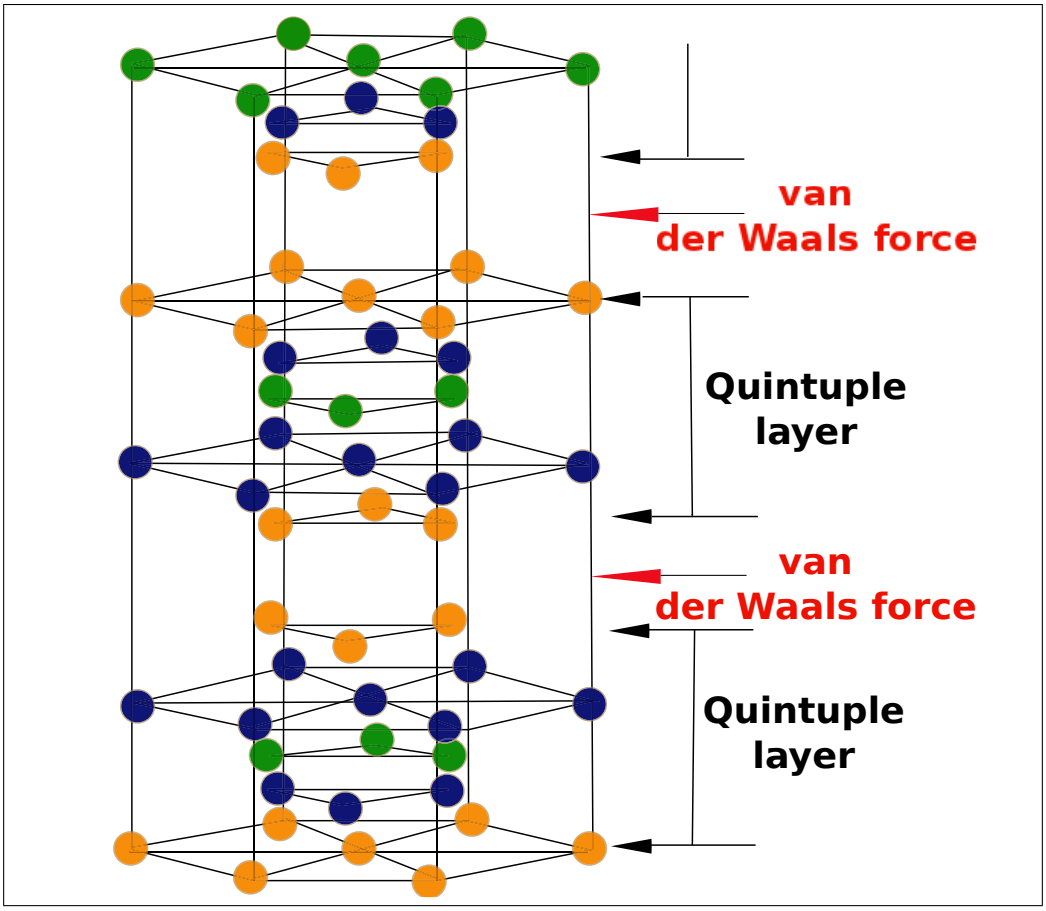

Figure 1.1: Schematic of Bi_2Te_3 crystal showing the arrangement of atoms and van-der-waals gap, with the orange, blue, green circles representing $Te^{(1)}$, Bi, $Te^{(2)}$ atoms respectively.

From the arrangement above, we see that the Bi atom is sandwiched between two Te atoms, with the $Te^{(2)}$ atom acting as an inversion centre. This centrosymmteric property of the crystal structure gives rise to mutually independent Raman and IR active modes, this will be explained in detail in a later section. The foregoing is obtainable for Bi_2Se_3, and Sb_2Te_3 as well.

Bulk crystals of these materials are relatively easy to grow, (a method of growth will be presented in Chapter 3 of this thesis). On the contrary, growing few-quintuple layered samples can be challenging due to the nanoscale of the quintuple layer. The two commonly used methods to date employed in growing few-quintuple layered samples are molecular-beam epitaxy and mechanical exfoliation of bulk samples using Scotch tape. The Scotch-tape mechanical exfoliation method has proven to be more efficient because it merely involves making thin samples from original bulk materials, so that the composition still remains the same. The weak van der Waals force holding layers together makes it possible to mechanically exfoliate thin layers from bulk samples of a couple of hundred microns in thickness [28, 29], similar to the case of graphene. Although exfoliated samples retain the composition and structure of bulk crystals, there is a change in phonon dynamics as one crosses to samples with nanoscale thickness. As a result, many vibrational mode studies done on these materials have been on few-QL samples [11, 18, 28–30]. In this thesis, the vibrational properties of bulk samples of Bi_2Se_3, Bi_2Te_3 and Sb_2Te_3, on which little work has been done will be explored.

1.1.2 2D semiconductors

2D semiconductors are another class of exotic materials that has widely studied in the last decade. Unlike conventional semiconductors (e.g., silicon), they have a layered structure, and owing to this, they exhibit properties that are dependent on the number of layers present, making it possible to deploy them in a wide range of applications.

Transition metal dichalcogenides (TMDCs) are a family of 2D semiconductors; Notable examples are $MoSe_2$, MoS_2, $MoTe_2$, WSe_2, WS_2, $TaSe_2$, $NbSe_2$. Their discovery came about after huge success was recorded in the study of the properties of graphene and boron nitride. Transition metal dichalcogenides have gained much attention in recent times from the scientific community. One reason is that in 2D they exhibit properties that suit some specific applications better than those of graphene [31, 32]. One such property is the presence of a band gap in transition metal dichalcogenides, making them suitable for usage in electronic devices unlike graphene where there is no band gap. Simply by controlling the layer thickness or by intercalation (insertion of an ion into compounds with layered structures) the material properties can be greatly altered.

One remarkable property of TMDCs is a transformation of an indirect band gap in the bulk to direct band gap for mono-layered samples as a result of a confinement effect [33]. The confinement effect arises when the size of a material is small in comparison to the wavelength of the electron, thereby causing a greater portion of the material to be in immediate contact with an interface, in this case air-sample interface. It has also been reported that inversion symmetry breaking together with spin orbit coupling as a result of going from bulk to mono-layered sample gives rise to an interplay of spin and valley degrees of freedom at the Dirac point of these materials [34].

The vibrational and elastic properties of WSe_2 will be discussed in this thesis. WSe_2 has found a wide range of applications as a lubricant at high temperatures and pressures, and in the fabrication of photoelectrochemical cells for solar energy conversion. Reports also has it that the intercalation of single crystals of WSe_2 with

alkali or alkaline earth metals results in a material with superconducting properties.

1.1.2.1 WSe_2

Tungsten diselenide, WSe_2, like other transition metal dichalcogenides, is a layered material that exhibits semiconducting properties. Bulk crystals can be considered as 3D when there are many layers stacked along the c-axis, while ultra-thin samples can be regarded as quasi-2D.

WSe_2 can exist in different structures called polymorphs. Common polymorphs of WSe_2 are 1T, 1H, 2H, 3R, where the letters denotes trigonal, hexagonal and rhombohedral respectively, and the digit represents the number of Se−W−Se units in the unit cell, each unit of Se−W−Se corresponding to a layer in the crystal. The 2H structure is the most widely studied of all three polymorphs. 2H-WSe_2 crystallizes in the D^4_{6h} space group. The unit cell has two layers of the crystal, with six atoms.

Like the 3D topological insulators, layers within single WSe_2 crystals are bonded by van der Waals forces making mechanical exfoliation to thin layers a possibility. WSe_2 in 2D has a high chemical and mechanical stability even though it is only a few nanometers thick. Similar to the 3D TIs, the phonon dynamics, and also the electronic properties, vary when going from 3D to 2D. One such electronic property is the transformation from an indirect band gap ($\approx$ 1.21 eV) in bulk samples to a direct band gap with a value of about 1.25 eV in mono-layered samples.

1.2 Vibrational and Elastic Properties

1.2.1 Raman Scattering Studies on Bi_2Se_3, Bi_2Te_3, Sb_2Te_3

Raman scattering has been tried and proved to be a reliable technique in materials science for probing vibrational modes in materials. This, in principle, it owes to its non-destructive, microscopic nature.

There have been only a few Raman scattering experiments conducted on both bulk and few-quintuple layered samples of Bi_2Se_3, Bi_2Te_3, and Sb_2Te_3. A thorough literature search shows that all of the Raman work was carried out between year 2012 and now, with most work reported for few-quintuple layered samples. We find there are some inconsistencies in the nature of the Raman active modes reported.

Group theory analysis reveals that there are 4 Raman active modes in these materials: $2A_{1g} + 2E_g$. A_{1g} represents out-of-plane (ab plane of the unit cell) vibrations and the E_g modes represents in-plane (ab) vibrations as shown in Figure 1.2.

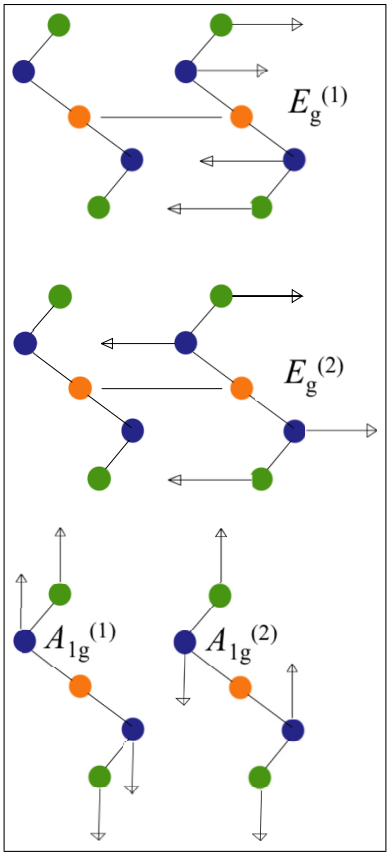

Figure 1.2: Displacement patterns of phonons. The E_g and A_{1g} modes involve displacement of atoms in the a-b plane and along the c axis respectively. Horizontal arrows signifies in-plane lattice vibrations while vertical arrows signifies out-of-plane lattice vibrations. The coloured circles are as represented in Figure 1.1.

Raman scattering studies of bulk samples of Bi_2Se_3, Bi_2Te_3, and Sb_2Te_3 performed by Richter *et al.* [21] produced three of the four expected Raman modes. In their report, they found good agreement between experimentally observed Raman shifts and those predicted by theory across all three materials. However, they observed that all of the calculated frequencies are lower than the experimental data for Bi_2Se_3, but

not for Bi_2Te_3 and Sb_2Te_3; the authors were of the opinion that there are stronger binding forces in Bi_2Se_3 than in Bi_2Te_3 and Sb_2Te_3.

Childres *et al.* [35] in their work on bulk Bi_2Se_3, Bi_2Te_3, and Sb_2Te_3, observed only two of the four predicted Raman modes, the other two modes that were not observed appeared at low frequency shifts, a region made inaccessible to probing due to a filter in their Raman set-up. The reported Raman shifts agreed well with those reported in previous literature [21]. Results of Raman scattering on plasma-etched samples were also presented. Employing different etching times produced samples with varying thickness. Raman scattering on these etched samples showed an increase in the width of spectral peaks as the etching time increased. This was attributed to a decrease in phonon lifetime, caused by increased phonon scattering in the sample.

Crystal symmetry breaking was observed in few-QL Bi_2Te_3 by Shahil *et al.* [19]. In their micro-Raman spectroscopy results of few-nanometer thick samples, they found the appearance of a new optical phonon mode A_{1u} which is not Raman active in bulk crystals. This A_{1u} mode, which is an infrared active mode, will only appear in a Raman scattering experiment in the absence of inversion symmetry in a crystal. The authors then reached the conclusion that the appearance of this mode in the Raman spectra of few-QL Bi_2Te_3 can only be as a result of broken centrosymmetry in atomically thin samples. Another trend that was observed was the growth in intensity of the A_{1u} peak due to a reduction in sample thickness, which resulted in the authors proposing that the evolution of Raman signatures with film thickness can be used in identification of crystals with the thickness of few-quintuple layers.

Zhao *et al.* [24] observed the emergence of the A_{1u} mode in the Raman spectra of Bi_2Se_3 nanocrystals thinner than 10 nm, while it appeared in crystals thinner than

84 nm in Bi_2Te_3. Their argument was that band bending (resulting from the ultra-thin nature of the samples) generates an electric field at the surface. The electric field which arises as a result of broken inversion symmetry on the surface is believed to coincide with the appearance of the A_{1u} mode in the Raman spectra. They also concluded that the thickness of nano-crystals of Bi_2Se_3 can be ascertained simply by a study of the intensities of the Raman active modes.

A comparative work done in few-quintuple layered samples across all three materials (Bi_2Se_3, Bi_2Te_3, and Sb_2Te_3) with thickness < 50 nm was reported in [19]. The authors observed the emergence of the A_{1u} mode in Bi_2Te_3 of about 50 nm thick. This optical mode was not observed in Bi_2Se_3 and Sb_2Te_3 of the same thickness, and not even when the thickness was reduced to about 8 nm. This result is contrary to what was reported in [24].

Kim *et al.* [36] also investigated the temperature dependence of Raman modes in Bi_2Se_3 and Sb_2Te_3 with a focus on the A_{1g} mode. They found that at temperatures above 90 K, the frequency and line width of this mode varies linearly with temperature. A complementary work to this was done by Bushra *et al.* [37] where all four Raman active modes in Bi_2Se_3 were observed. The temperature dependences of the vibrational modes ware found to be almost linear and the full widths at half maximum of the peaks were observed to increase with temperature. They also estimated the temperature coefficients for the $A_{1g}^{(1)}$, $A_{1g}^{(2)}$ and $E_g^{(2)}$ Raman active modes.

In the work by Zhang *et al.* [25] on Bi_2Se_3 nanoplatelets, all four predicted Raman modes were observed. One out of the two out-of plane A_{1g} was observed to red shift as thickness decreased. They argued that the shift in frequency was due to a decrease in interlayer van der Waals force which effectively leads to a decrease in the restoring

force acting on the atoms as thickness decreases. A broadening of the line width of the E_g mode was also observed as the number of quintuple layers decreased. From their results, they concluded that there exists a marked difference between the effect of electron-phonon coupling in bulk and that in atomically thin Bi_2Se_3.

Teweldebrhan *et al.* [29] observed that in suspended atomically-thin films of Bi_2Te_3, the out-of-plane vibrations had higher intensity compared to thin films of same thickness that were supported by silicon/SiO_2 substrate. The appearance of the A_{1u} mode was also reported. The appearance of the A_{1u} peak in multi-quintuple Bi_2Te_3 film (thickness $\simeq$ 50 nm) was also reported by Goyal *et al.* [38].

Density functional perturbation theory (DFT) was employed in calculating the Raman spectra of Sb_2Te_3 by Sosso *et al.* [39]. Good agreement was found with experimental data. Cheng and Shang-Fen [40] in studying the role played by spin-orbit coupling on the phonon dynamics of single-quintuple Bi_2Te_3 and Bi_2Se_3 films, calculated Raman shifts with and without spin-orbit coupling. They found that the presence of spin-orbit coupling had more effect on the in-plane lattice vibrations than it had on the out-of-plane vibrations.

In summary, the foregoing results show that there are some inconsistencies in the Raman scattering studies of the vibrational properties of Bi_2Se_3, Bi_2Te_3, Sb_2Te_3. The appearance of an infrared-active mode has been reported in few-QLs of Bi_2Te_3 and Bi_2Se_3 by some authors while this signature was only reported for Bi_2Te_3 by others. The intensity of the spectral peaks has also been a major point of debate. Some authors reported that the A_{1g} mode has a lower intensity than the E_g mode across all three materials, while other authors report contradictory results.

1.2.2 Raman Scattering Studies on WSe_2

The assignment and nature of the vibrational modes in WSe_2 has generated a lot of controversy since the first Raman work was reported by Mead *et al.* [41]. Some authors have also reported the appearance of second-order Raman modes while such modes did not show up in the work undertaken by others [33, 41, 42]. Of the 18 vibrational modes at the Brillouin zone centre of 2H-WSe_2, four of these are Raman active modes:

$$A_{1g} + E_{1g} + E_{2g}^{(1)} + E_{2g}^{(2)}.$$

Only three of these modes are observable in a backscattering geometry, with the E_{1g} mode absent. An extensive study of the confinement effect on electronic and excitonic dispersion in thin sheet WSe_2 crystals has yielded a consensus on the role played by confinement effect in this material. However, the same effort has not been spent on phonon dynamics. Mead *et al.* [41] presented a study of first-order Raman spectrum of WSe_2 using both the backscattering and 90° geometries. By so doing, they were able to observe all four Raman active modes. Using a scaling law, the frequencies of the observed modes were compared to the values obtained in MoS_2, and showed good agreement.

Sahin *et al.* [33] observed that in bulk samples of WSe_2 there is one prominent spectral peak at 252.2 cm^{-1}. On the contrary, typical Raman spectra of other members of the transition metal dichalcogenide family display two very strong distinct spectral peaks: $E_{2g}^{(1)}$, A_{1g}, and a small peak, $E_{2g}^{(2)}$. Sahin *et al.* stated that the $E_{2g}^{(1)}$, and A_{1g} are degenerate in bulk WSe_2 resulting in the prominent peak at 252.2 cm^{-1}. Consequentially, there is an anomaly in the phonon dispersion of WSe_2. It was con-

firmed in the same paper through a calculated phonon dispersion that there indeed exists only one strong vibrational mode at about 250 cm^{-1}. Interestingly, on going from 3D to 2D (thinner samples), the degeneracy is lifted and the prominent peak splits into two (A_{1g} and $E^{(1)}_{2g}$ modes). Contrary to this, the calculated phonon dispersion showed that the degeneracy is independent of dimensionality [33].

Zhao *et al.* [43] observed in the Raman spectra of monolayer WSe_2 that the A_{1g} and $E^{(1)}_{2g}$ mode are degenerate as predicted by the theoretical calculations for monolayer crystals done by Sahin *et al.* [33]. On the contrary, a lifting of the degeneracy was observed in multilayered samples. Another feature observed in their spectra was a strong dependence of Raman features of WSe_2 on excitation conditions due to energy-dependent Raman cross-section of phonons.

Raman scattering experiments on nanofilm WSe_2 studied by Wang *et al.* [44] showed the $E^{(1)}_{2g}$ and A_{1g} are almost indistinguishable due to their close Raman shifts at 250 cm^{-1} and 253 cm^{-1} respectively. Similar results were obtained in terms of position and shape of the spectral peaks with WSe_2 nanofilms on silicon nanowire as substrate, showing that the choice of substrate had little or no effect on the nature of the spectral peaks.

Tonndorf *et al.* [42] showed that there are two distinct Raman signals at 248 cm^{-1} and 250.8 cm^{-1} for bulk WSe_2, while they found only a single spectral peak in few-layer samples, the position of which changes with the number of layers. They were not able to ascertain whether the observation of a single peak in few-layered sample had to do with a degeneracy of modes.

1.2.3 Elastic Properties Studies of 2H-WSe_2

There have been no reported experimental studies of the elastic properties of 2H-WSe_2, and only one [45] that explored these properties using a theoretical approach. Feng *et al.* [45] reported first-principles calculations of the equilibrium lattice parameters and elastic constants of WSe_2 at 0 GPa, however no mention of the surface acoustic phonons was made. There is only one report of an experimental study using the same technique employed in this thesis to study the elastic properties of closely related materials. In the Brillouin scattering studies conducted by Harley and Fleury [46] on related materials; $TaSe_2$ and $NbSe_2$; the velocities of surface and bulk acoustic waves were obtained.

1.3 Motivation for the Present Work

The present work consists of three parts: first, Raman spectroscopy has been used to study the vibrational properties of bulk samples of Bi_2Se_3, Bi_2Te_3, Sb_2Te_3, and WSe_2. In the case of the topological insulators Bi_2Se_3, Bi_2Te_3, and Sb_2Te_3, there have been a few studies, most of which have been on few QLs samples. There have also been some inconsistencies in the appearance of a new optical phonon mode as the inversion symmetry in these materials is broken. An infrared active mode A_{1u} has also been observed in the Raman spectrum of few QL Bi_2Te_3 [19, 29] but not in Bi_2Se_3 or Sb_2Te_3, while this mode was observed in Bi_2Se_3 [24]. There is also a lack of consensus on the variation of intensity of the Raman active mode with sample. A quantitative study of the nature of the Raman active modes in bulk and mechanically exfoliated samples of Bi_2Se_3, Bi_2Te_3, and Sb_2Te_3 is presented in this

work. The samples used were a few hundred microns thick. Polarization studies were employed to assign phonon modes. All of these culminated in a robust report on Raman scattering experiments in Bi_2Se_3, Bi_2Te_3, and Sb_2Te_3.

Second, in 2H-WSe_2, previous Raman scattering studies have been far from consistent. The degeneracy of phonon modes, the frequency shifts at which phonon modes appear, and the origin/presence of second order Raman modes have been major topics of debate. The present work aims to address these inconsistencies by offering an in-depth study of the nature of the vibrational modes. Polarization studies of the Raman modes were done, enabling us to correctly assign the observed spectral peaks and their frequencies. It is worth mentioning that all of the Raman work reported here was carried out with an excitation wavelength in the near-IR region, different from the wavelength(s) used by other authors.

Brillouin scattering experiments have been used to study the elastic properties of 2H-WSe_2. There are no previous experimental reports on the elastic properties of this material. The velocity of the Rayleigh surface acoustic wave was determined and compared with those of some members of the transition metal dichalcogenide family.

This work was borne out of the need to resolve the existing inconsistencies reported in previous studies on some of the vibrational properties of Bi_2Se_3, Bi_2Te_3, Sb_2Te_3, and WSe_2. The present work is also intended to report new results of the vibrational properties of these materials.

Chapter 2

Theory

2.1 Inelastic light scattering in crystals

A typical light scattering experiment involves five main parts: an incoming beam, a target, a scattered beam, a detector, and a spectrometer for frequency analysis. The target, which could be atoms of a crystal or a molecule, scatters the incoming beam in all directions. If the energy of the scattered wave differs from that of the incident wave, the scattering is referred to as inelastic scattering, while if it is the same it is called elastic scattering. Our concern here is on inelastic scattering because Raman scattering and Brillouin scattering are of this type.

2.1.1 Basic Concepts

Inelastic light scattering is regarded as a process whereby photons of light are scattered by a medium (e.g. a crystal) with the simultaneous creation or annihilation of phonon(s) within the medium [47]. If laser light with photons of energy $\hbar\omega_i$ and

momentum $\hbar\vec{k}_i$ is scattered by phonons in a crystal to produce scattered light of energy $\hbar\omega_s$ and momentum $\hbar\vec{k}_s$, with the creation or destruction of phonons of energy $\hbar\omega$ and momentum $\hbar\vec{q}$, energy and momentum will be conserved,

$$\hbar\omega_i - \hbar\omega_s = \pm\hbar\omega \tag{2.1}$$

$$\hbar\vec{k}_i - \hbar\vec{k}_s = \pm\hbar\vec{q} \tag{2.2}$$

where ω and k are the angular frequency and wave vector respectively with subscript i and s representing incident and scattered components. The sign of the term on the right hand side of equations (2.1) and (2.2) tells us whether the process involves the creation or annihilation of a phonon. When positive, it corresponds to the process of phonon annihilation, also know as an anti-Stokes process; on the other hand if negative, it implies the creation of a phonon, otherwise called a Stokes process. In either case, the absolute value of the frequency (and wave vector) is the same.

2.2 Lattice Vibrational Modes

The atoms in a crystal are understood to be constantly vibrating about their equilibrium positions. The movement of the atoms is constrained by the symmetry of the crystal lattice. Motion can be inhibited in some directions and enhanced in others depending on the positions of neighbouring atoms. When atoms in a crystal vibrate with the same frequency and a fixed phase relation, it results in a normal mode. If the atoms in one unit cell move in phase with respect to atoms in a neighbouring unit cell, such a vibration is termed an acoustic mode. On the contrary, if atoms of a unit cell move in opposite directions with respect to each other an optical mode is formed.

A plot of the frequency, $\omega(k)$ versus the phonon wave vector k (which is called a phonon dispersion curve) in the first Brillouin zone shows the nature of both kinds of phonon modes. The dispersion relation at small values of k for acoustic mode is linear, $\omega \simeq kv$, which is characteristic of sound waves with velocity v, whereas the optical modes exhibit a lower dispersion of k with respect to ω (smaller slope), as shown in the phonon dispersion curve in Figure 2.1.

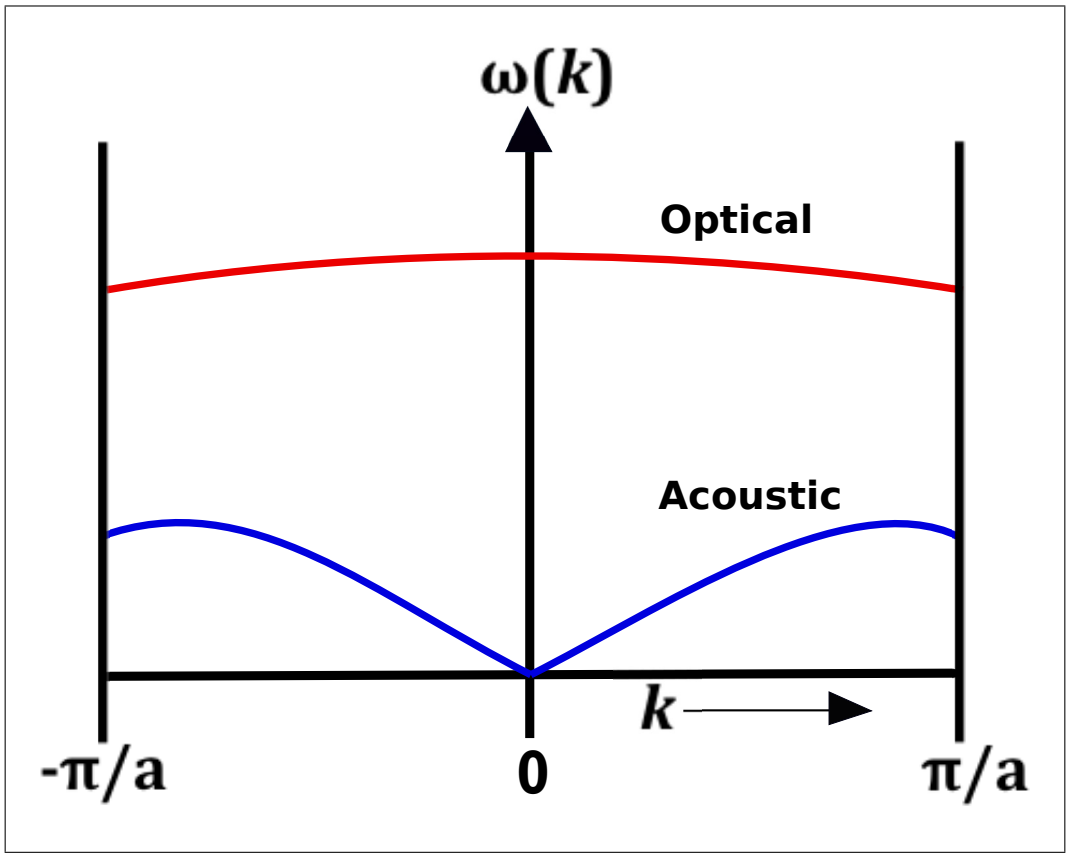

Figure 2.1: Phonon dispersion curve showing acoustic and optical phonons

In a crystal with n atoms/unit cell, the number of vibrational modes for any given wave vector is $3n$. There are 3 acoustic modes and $3n-3$ optical modes. For instance,

in a monoatomic crystal ($n = 1$), there are three acoustic modes with no optical modes. The three acoustic modes consist of one longitudinal and two transverse modes.

For Brillouin and Raman scattering, we usually consider phonon modes at $k \simeq 0$. The reason for this is because the phonon wave vector π/a (where a is the lattice constant) is significantly greater than the photon wave vector π/λ; in other words, the magnitude of the vibrational wave vector k is typically small compared to the Brillouin zone boundary wave vector π/a. We are allowed to make the assumption that $k \simeq 0$ (corresponding to infinite wavelength limit) provided that $\lambda \gg a$.

2.2.1 Brillouin Light Scattering

Brillouin light scattering (BLS) is a process that involves the scattering of photons by thermally excited acoustic phonons. Information about the elastic and photo-elastic properties of the material being studied can be gathered from BLS experiments. This technique has been used to study transparent, translucent and opaque materials.

Two mechanisms are involved in light scattering by acoustic phonons [48]. First there is an elasto-optic scattering mechanism, where fluctuations in the strain field causes fluctuations in the dielectric constant, which brings about fluctuations in the sample refractive index. This mechanism occurs in the bulk (order of a few hundred microns) of the sample. The second mechanism, which is a surface effect, is called the surface ripple effect. It is caused by deformations on the sample surface which scatters incident light with a Doppler shift. In general, a typical Brillouin spectrum should contain information about both bulk and surface acoustic phonons, but this is contingent on the nature of the material being probed.

The three most commonly used geometries in a BLS experiment are backscattering geometry (180^0), 90^0 geometry and platelet geometry. In opaque materials, the backscattering geometry often yields the most useful results. In the arrangement shown in Figure 2.2, the phonon wave vector $\vec{q}$ in equation (2.2) can be written in components parallel and perpendicular to the surface as

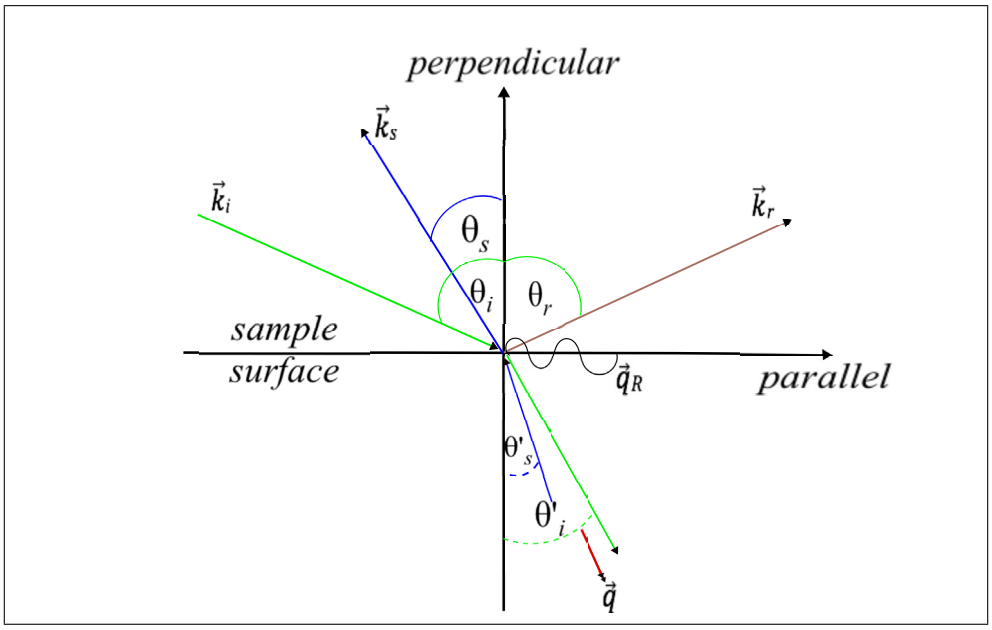

Figure 2.2: Schematic of the scattering geometry showing incident, reflected, and scattered light wave vectors $\vec{k}_i$, $\vec{k}_r$ and $\vec{k}_s$, and the bulk and surface phonon vectors $\vec{q}$ and $\vec{q}_R$ respectively.

$$q_{\parallel} = k_i \sin\theta_i + k_s \sin\theta_s \tag{2.3}$$

$$q_{\perp} = n(k_i \cos\theta'_i + k_s \cos\theta'_s), \tag{2.4}$$

where θ_i and θ_s are incident angle and the angle the scattered light makes with

sample normal outside material respectively measured on the material surface from the normal to the surface, θ_i' and θ_s' are angles the incident and scattered light make inside the material measured from the normal to the surface, $\sin\theta_i = n\sin\theta_i'$, $\sin\theta_s = n\sin\theta_s'$ and n is the refractive index of the material. The frequency shift f_B of the scattered light and the magnitude of the wave vector q are related by

$$\omega_B = qV_B, \tag{2.5}$$

$$f_B = \frac{\omega_B}{2\pi} = \frac{qV_B}{2\pi} \tag{2.6}$$

where V_B is the bulk acoustic phonon velocity. The foregoing is what goes on in the bulk.

For surface phonons, the expression (2.4) does not apply, since $q_\parallel$=q_R where q_R is the surface phonon wave vector. Using the general relationship between the magnitude of incident and scattered wave vectors, $|k_i| = |k_s|$ and $\theta_i = \theta_s$= θ, for backscattering geometry such as that used in the present work, equation (2.3) becomes

$$q_\parallel = q_R = 2k_i\sin\theta. \tag{2.7}$$

The expression (2.5) also applies to surface phonons except that the velocity in this case will be surface acoustic phonon velocity,

$$\omega_R = q_R V_R, \tag{2.8}$$

which then reduces to

$$f_R = \frac{\omega_R}{2\pi} = \frac{2k_i V_R\sin\theta}{2\pi} = \frac{2V_R\sin\theta}{\lambda_i}, \tag{2.9}$$

where λ_i= $\dfrac{2\pi}{k_i}$ is the wavelength of the incident light.

2.2.2 Raman scattering

Raman scattering is a type of inelastic scattering experiment which probes the optical phonons in a material, which invariably means that Raman scattering involves a change in light energy. This change in light energy in Raman scattering reported in wave number units is usually of the order ≥ 1 cm^{-1}. Raman scattering was first observed by C. V. Raman in 1928. It was first applied to the study of liquids before finding its way to the study of a variety of molecules and crystals. A review of the Raman effect in crystals can be found in Loudon [49]. Other techniques have evolved from basic Raman spectroscopy including resonance Raman spectroscopy, surface-enhanced Raman spectroscopy, spontaneous Raman spectroscopy, and hyper-Raman spectroscopy.

In the classical model, when an electric field that varies with time as

$$E = E_0 \cos \omega_i t, \tag{2.10}$$

where E_0 is the amplitude of the electric field incident on a crystal, an electric dipole moment P is induced in the target crystal,

$$P = \alpha E = \alpha E_0 \cos \omega_i t, \tag{2.11}$$

where α is the polarizability, a second rank tensor [50]. The atoms of the crystal, initially vibrating with a frequency ω_L, have their displacement from equilibrium position given by

$$r = r_0 \cos \omega_L t, \tag{2.12}$$

where r_0 is the vibrational amplitude. We can express α as a linear function of r as

$$\alpha = \alpha_0 + \left(\frac{\partial \alpha}{\partial r}\right)_0 r + \ldots, \tag{2.13}$$

where α_0 is the polarizability at equilibrium position and $\left(\frac{\partial \alpha}{\partial r}\right)_0$ is the rate of change of α with respect to change in position r evaluated at the equilibrium position. Substituting (2.12) into (2.13) we find

$$\alpha = \alpha_0 + \left(\frac{\partial \alpha}{\partial r}\right)_0 r_0 \cos \omega_L t + \ldots, \tag{2.14}$$

Combining (2.14) and (2.11), we get

$$P = \alpha_0 E_0 \cos \omega_i t + \left(\frac{\partial \alpha}{\partial r}\right)_0 r_0 E_0 \cos \omega_i \cos \omega_L t + \ldots, \tag{2.15}$$

which on applying the trigonometry identity:

$$\cos A \cos B = \tfrac{1}{2} \cos(A - B) + \tfrac{1}{2} \cos(A + B),$$

becomes

$$P = \alpha_0 E_0 \cos \omega_i t + \frac{1}{2}\left(\frac{\partial \alpha}{\partial r}\right)_0 r_0 E_0 \Big(\cos(\omega_i - \omega_L)t + \cos(\omega_i + \omega_L)t \Big) + \ldots \tag{2.16}$$

The first term in the above expression represents an oscillating dipole that radiates light of frequency ω_i (elastic scattering), the second term corresponds to Raman activity with $(\omega_i - \omega_L)$ as the Stokes process and $(\omega_i + \omega_L)$ the anti-Stokes process discussed in section (2.1). The second term corresponds to a change in frequency, which is the term that leads to Raman scattering. The condition for Raman active vibrations is therefore that $\left(\frac{\partial \alpha}{\partial r}\right) \neq 0$; if this term is zero, we will be left with only the first term in equation (2.16). It is worth mentioning that equation (2.16) has been limited to the first-order Raman effect; higher order terms have been omitted for

simplicity. The Stokes lines are usually stronger than the anti-Stokes lines. Since both provide the same information, those of the Stokes are usually examined in experiments because of their higher intensity. The intensity of the peak due to a Raman active mode is dependent on the polarizability of the crystal and the incident electric field. Resonance effects arising from the choice of the laser excitation wavelength can also enhance the intensity of a Raman peak. If the energy of the incident light source corresponds to energy of a vibrational mode in the crystal which is Raman active, the intensity of the peak due to the Raman active mode is enhanced accordingly.

Not all vibrations in a crystal will result in Raman scattering, in other words, not all vibrations are Raman active. The rules governing the modes that will be seen in a Raman experiment are called selection rules, this will be explained in detail in Section 2.3.3.

2.3 Group Theory as a Tool in Raman Spectroscopy

Application of the mathematical theory of groups (group theory) to the symmetry of crystals is a powerful method that allows for a quantitative description of the crystal vibrational properties. A prediction and classification of the vibrational modes found in infrared and Raman spectra can be obtained by group theory analysis. In the following, a few concepts that apply to symmetry will be discussed.

2.3.1 Symmetry, Point groups and Space groups

The symmetry operations of a crystal are particular operations that leave the crystal invariant. In other words, there is no difference in the appearance of the crystal before and after performing such operation(s). A set/group of symmetry operations whose operation leaves at least one point in a crystal unmoved is called a *point group*. This group excludes any form of lattice translations. When translations are included, a new group called a *space group* is formed [51]. There are 32 crystallographic point groups and 230 space groups as listed in the International Table for Crystallography [52].

A few examples of point group operations are: the identity (E); n-fold rotation (C_n) which is a rotation by angle $2\pi/n$; reflection (σ) through a plane, inversion (i) which is a reflection of each point through a point .

An operation of the space group S can be expressed mathematically as

$$\{R|t + t'\},$$

where R represents a point group operation, t is a lattice translation and t' is a fraction of a lattice translation. 73 out of the 230 space groups have no fractional translations; they are called *symmorphic*, while the other 157 are called *non-symmorphic*. The set of operations with no translations is the point group G, and $\{E|0\}$ is the identity element [51].

The notation $\{E|t\}$ represents a pure translation. The group of translations is a subgroup of the space group. A subgroup is a collection of elements within a group that forms a group.

There are three common notations used to express the space group of a crystal;

the first is by number, where each space group is given a number from 1 to 230; the other one is the International symbol or Hermann-Mauguin notation which describes the Bravais lattice followed by the most prominent symmetry operations, and lastly the Schönflies notation. In this thesis, we will use the Schönflies notation with the other notations given in parentheses.

Bi_2Se_3, Bi_2Te_3, and Sb_2Te_3 belong to the space group D_{3d}^5 ($R\bar{3}m$, No. 166). The D represents a dihedral rotation group, the '3' represents the principal rotation axis which is three-fold in this case, the d implies a mirror plane parallel to the three-fold principal rotation axis, the '5' simply represents the fifth space group of the D_{3d} group. WSe_2, on the other hand belongs to space group D_{6h}^4 ($P6_3/mmc$, No. 194). The '6' implies that the principal axis a six-fold rotation axis and the h implies there is a mirror plane perpendicular to the six-fold rotation axis.

2.3.2 Representations and Character Tables

The order of a group is defined as the number of elements in the group. In a finite group (*i. e.* one that has a number of finite elements), the products of elements of the group can be ordered into a table known as a group multiplication table. Performing the operations necessary to obtain the products of the elements of a group may be cumbersome due to the individual elements of a group being complex or abstract. This can be resolved by finding another group whose multiplication table is known and whose symmetry operations have a one-to-one correspondence with that of the original group. This property, which is called isomorphism, helps simplify the problem of complexities in obtaining the multiplication table of a group [53]..

If there exists a correspondence between the elements of a group X with those of an arbitrary group Y whose elements are numbers or matrices, we say that the group Y is a *representation* of the original group. Representations can be described in terms of their dimension, which is the order of square matrices that constitute it. If the elements of the representation are simply numbers, then its dimension is 1. Typically one can take two or more representations and construct a new representation by combining the matrices into larger matrices, the larger matrices form a reducible representation. Put another way, if the matrices in the representation of a group can be diagonalised (put in a block form), then the representation is reducible otherwise it is irreducible [53].

The character of a matrix representation is the trace (sum of diagonal elements) of that matrix. Information on the characters of the representation of a group can be summarized in a character table. Each of the 32 crystallographic point groups has a character table that expresses the symmetry operations as well as the irreducible representations under each point group. Also included in this character table is how each irreducible representation transforms the coordinate system. These transformations come in handy in telling the nature of the vibrational modes of the atoms of a crystal or molecule, whether a particular mode is IR active or Raman active or both. The D_{3d} point group character table of Bi_2Se_3, Bi_2Te_3, and Sb_2Te_3 is as shown below.

The first line contains all the symmetry operations that make up the point group. Each of the other rows that follow contains the characters of the irreducible representations of the group, with each row beginning with a label for the irreducible representation. The symbol A represents a one-dimensional representation, E represents a two-dimensional representation, the subscripts 1 or 2 denotes the representation

Table 2.1: Character table of the point group D_{3d}.

$\boldsymbol{D_{3d}}$	E	$2C_3$	$3C_2$	i	$2S_6$	$3\sigma_d$	linear functions, rotations	quadratic functions
A_{1g}	1	1	1	1	1	-1		x^2+y^2, z^2
A_{2g}	1	1	-1	1	1	-1	R_z	
E_g	2	-1	0	2	-1	0	(R_x, R_y)	(x^2-y^2, xy), (xz, yz)
A_{1u}	1	1	1	-1	-1	-1		
A_{2u}	1	1	-1	-1	-1	1	z	
E_u	2	-1	0	-2	1	0	(x, y)	

that is symmetric or antisymmetric respectively with respect to rotations about the C_2 rotation axis, the g or u subscript stands for representation that is symmetric or antisymmetric respectively with respect to the inversion centre. The two right-most columns provide information on how the irreducible representation transforms the coordinate system, these columns are very useful when assigning vibrational modes.

2.3.3 Characters of Vibrational Modes and Factor Groups

The vibrational modes of a crystal may each be associated with the irreducible representations of the crystallographic space group. This relationship between vibrational modes and the irreducible representations of the space group forms the basis of the application of group theory to vibrational spectroscopy.

Group theory, as a mathematical tool, employs the concept of symmetry to describe vibrational spectra. One can get information such as the number of modes expected to be found in an infrared or Raman spectroscopy experiment, and polar-

ization dependence among other things. Our main focus is to employ the concepts of group theory through the factor group analysis in predicting and assigning Raman active modes accordingly.

Next we make some definitions which will lead us to understanding the concept of a factor group. One such definition is that of a subgroup. The group formed by any subset of elements within a larger group G is referred to as a subgroup of the larger group. A subgroup Ω is invariant if

$$X^{-1}\Omega X = \Omega,$$

for all elements X in the group G. The above expression can be expressed in another form if it is multiplied from the left hand side by X and using the property that $X^{-1}X = 1$,

$$\Omega X = X\Omega.$$

In other words, the left and right coset of an invariant subgroup are identical. For such an invariant subgroup, another group called a factor group can be formed from it with elements that are cosets of the invariant subgroup. An interesting property of the factor group is that it is isomorphic to the crystallographic point group, and also the fact that its irreducible representations can be used in working out the normal modes.

The factor group method, which was discovered in 1969 by Bhagavantam and Venkatarayudu [54], gives an analysis of the vibrations at the Brillouin zone centre ($k = 0$). The following discussion follows from the derivations in [54]. The condition $k \simeq 0$ limits the available Raman information to just first-order Raman scattering. To obtain information about higher order Raman scattering, a complete analysis over

the entire Brillouin zone is necessary. Provided the space group and the Wyckoff positions of the atoms in a crystal (positions where atoms are seated within the unit cell) are known, information about the vibrational modes can be extracted. A prior knowledge of the Wyckoff positions is therefore imperative. Through it, the site symmetry (point group of the site) of the position where an atom is seated in a crystal can be deciphered, from which the character for each class of symmetry operation can be worked out using

$$\chi_\rho = \omega_\rho(\pm 1 + 2\cos\theta), \tag{2.17}$$

where ω_ρ represents the number of atoms whose positions are invariant during the operations of class ρ, and θ is the angle of rotation (since every symmetry operation, be it inversion $\theta = 180\,^\circ$ or reflection $\theta = 0\,^\circ$ can be treated as a rotation) [54]. This simplifies the problem of analyzing symmetry properties to that of determining the invariance conditions of the unit cell. The positive sign in equation (2.17) stands for proper rotation while the negative term for improper rotations. The number of atoms ω_ρ, which remain fixed during an operation of a class ρ can be found from

$$\omega_\rho = \frac{g}{m}\frac{m_\rho}{g_\rho}, \tag{2.18}$$

where g is the order of the factor group; m is the order of M, the point symmetry of the site group; g_ρ is the number of elements in the class ρ in M; m_ρ is the number of elements in the class ρ in the factor group [55].

After obtaining the set of reducible characters χ_ρ, the group theory theorem can be applied to calculate the distribution of the normal modes

$$n_i = \sum_\rho \frac{1}{g}\chi_\rho g_\rho \chi_\rho{}^i, \tag{2.19}$$

where n_i is the number of times the ith irreducible representation is contained in the reducible representation; χ_ρ is the reducible character for each class ρ; ${\chi_\rho}^i$ is the character of class ρ in the ith representation [55].

As an illustration of the factor group analysis, we obtain the normal modes of the crystals studied in this thesis. First for 2H-WSe_2, whose space group is D^4_{6h}, we expect 18 (3 x 6) vibrational modes, since there are 6 atoms in its unit cell. Table 2.2 shows the atomic (Wyckoff) positions of WSe_2 as given by [56].

Table 2.2: WSe_2 Wyckoff Positions

Atom	Multiplicity	Wyckoff Letter	Site Symmetry
W	2	c	D_{3h} $(\bar{6}m2)$
Se	4	f	C_{3v} $(3m.)$

The point group D_{6h} of WSe_2 has order 24 (*i.e.* there are 24 symmetry operations contained in this point group), so that $g = 24$ for D_{6h} point group. The point symmetry of the W atom site is D_{3h} with $m = 12$ (order of site group), and that of the two Se atoms site is C_{3v} with $m = 6$ (order of site group). On applying equations (2.17) and (2.18) and noting that $g_\rho = m_\rho$ for all classes in this example, we obtain the following results

Table 2.3: Group theory calculations for WSe_2.

$\boldsymbol{D_{6h}}$	E	$2C_6$	$2C_3$	C_2	$3C_2'$	$3C_2''$	i	$2S_3$	$2S_6$	σ_h	$3\sigma_d$	$3\sigma_v$
2(c), D_{3h}	E	-	$2C_3$	-	$3C_2'$	-	-	$2S_3$	-	σ_h	-	$3\sigma_v$
W atom	2	-	2	-	2	-	-	2	-	2	-	2
4(f), C_{3v}	E	-	$2C_3$	-	-	-	-	-	-	-	-	$3\sigma_v$
Se atom	4	-	4	-	-	-	-	-	-	-	-	4
ω_ρ	6	-	6	-	2	-	-	2	-	2	-	6
χ_ρ	18	-	0	-	-2	-	-	-4	-	2	-	6

Table 2.3 shows how the calculations of the reducible characters is obtained. The first row is simply the D_{6h} point group and its symmetry operations. The first element of the second row shows the multiplicity+Wyckoff letter and site symmetry of the W atom, the symmetry operations of the site symmetry/point group (D_{3h}) are shown to the right of the first column, after which the equation for ω_ρ is used for each element of the point group. This process is repeated for the Se atom, and then the sum of ω_ρ for both atoms (W and Se) is obtained. The last row shows the value of χ_ρ for each operation on applying equation 2.17.

We then apply equation (2.19) and the irreducible representations of the D_{6h} character table shown in Table 2.4 to obtain the number of each of the irreducible representations contained in the reducible representation obtained in the table above. The irreducible representations/ vibrational modes are therefore

$$\Gamma_{irre} = A_{1g} + 2A_{2u} + B_{1u} + 2B_{2g} + E_{1g} + 2E_{1u} + E_{2u} + 2E_{2g}.$$

Table 2.4: Character table of the point group D_{6h}.

$\boldsymbol{D_{6h}}$	E	$2C_6$	$2C_3$	C_2	$3C_2'$	$3C_2''$	i	$2S_3$	$2S_6$	σ_h	$3\sigma_d$	$3\sigma_v$	Linear, rotations	Quadratic
A_{1g}	1	1	1	1	1	1	1	1	1	1	1	1		x^2+y^2, z^2
A_{2g}	1	1	1	1	-1	-1	1	1	1	1	-1	-1	R_z	
B_{1g}	1	-1	1	-1	1	-1	1	-1	1	-1	1	-1		
B_{2g}	1	-1	1	-1	-1	1	1	-1	1	-1	-1	1		
E_{1g}	2	1	-1	-2	0	0	2	1	-1	-2	0	0	(R_x, R_z)	(xz, yz)
E_{2g}	2	-1	-1	2	0	0	2	-1	-1	2	0	0		(x^2-y^2, xy)
A_{1u}	1	1	1	1	1	1	-1	-1	-1	-1	-1	-1		
A_{2u}	1	1	1	1	-1	-1	-1	-1	-1	-1	1	1	z	
B_{1u}	1	-1	1	-1	1	-1	-1	1	-1	1	-1	1		
B_{2u}	1	-1	1	-1	-1	1	-1	1	-1	1	1	-1		
E_{1u}	2	1	-1	-2	0	0	-2	-1	1	2	0	0	(x, y)	
E_{2u}	2	-1	-1	2	0	0	-2	1	1	-2	0	0		

Using the property that both the A and B modes have dimension 1 and the E modes have a dimension of 2, the number of vibrational modes add up to 18, as expected for 2H-WSe_2. The next step is to determine the modes that are Raman active, of which there are 4. This can be done by employing a set of rules for each irreducible representation of the factor group called selection rules. These sets of rules are used in determining which vibrational mode is Raman active and which is infra-red active by studying the transformation properties of the polarizability tensor and dipole moment operator, respectively. The polarizability tensor (responsible for Raman mode) transforms as a product of coordinates (e.g. xy, yy) in other words, quadratic, while the dipole moment (responsible for Infra-red mode) transforms as x, y or z, in other words, linear. This information is contained in the columns labelled linear/rotation and quadratic of a point group character table. The Raman active modes are therefore $A_{1g} + E_{1g} + 2E_{2g}$.

Now we consider the Raman active modes for Bi_2Se_3, Bi_2Te_3, Sb_2Te_3 with space group D^5_{3d}. The same Wyckoff positions and vibrational modes are common to all three crystals so we only consider for Bi_2Te_3. Since there are 5 atoms per unit cell of Bi_2Te_3, 15 vibrational modes are expected. The atomic positions are as given by [57] are shown in Table 2.5

Table 2.5: Bi_2Te_3 Wyckoff Positions

Atom	Multiplicity	Wyckoff Letter	Site Symmetry
$Te^{(2)}$	1	a	$\bar{3}$ m (D_{3d})
$Te^{(1)}$	2	c	3 m (C_{3v})
Bi	2	c	3 m (C_{3v})

The point group D_{3d} (of Bi_2Se_3) has order 12. The point symmetry of the $Te^{(2)}$ atom site is D_{3d}, the same as that of the crystal. This implies that this atom is seated at the highest symmetry position in the crystal, which is defined to be at the origin. The $Te^{(1)}$ site has the same point symmetry as the two Bi atoms, which is C_{3v} with order 6. On proceeding as was done for WSe_2 and applying equations (2.17) and (2.18), we obtained the following results

Table 2.6: Group theory calculations for Bi_2Te_3.

$\boldsymbol{D_{3d}}$	E	$2C_3$	$3C_2'$	i	$2S_6$	$3\sigma_d$
1(a), D_{3d}	E	$2C_3$	$3C_2'$	i	$2S_6$	$3\sigma_d$
$Te^{(2)}$ atom	1	1	1	1	1	1
2(c), C_{3v}	E	$2C_3$	-	-	-	$3\sigma_d$
$Te^{(1)}$ atom	2	2				2
2(c), C_{3v}	E	$2C_3$	-	-	-	$3\sigma_d$
Bi atom	2	2				2
ω_ρ	5	5	1	1	1	5
χ_ρ	15	0	-1	-3	0	5

The columns and rows in Table 2.6 follow the same explanation given for WSe_2. We then apply equation (2.19) to solve for the irreducible representation to obtain

$$\Gamma_{irre} = 2A_{1g} + 2E_g + 3A_{2u} + 3E_u.$$

Subsequently, the character table for the D_{3d} point group in Table 2.1 is used to determine that the Raman active modes are $2A_{1g} + 2E_g$. This concludes the application of group theory in predicting vibrational modes.

Knowing the nature of the Raman active modes is key in identifying them with peaks in a Raman spectrum. Theoretically, each Raman active mode has a characteristic behaviour peculiar to it. The A_{1g} modes for instance are a one-dimensional representation, and usually out-of-plane vibrations, while the E_g modes are two-dimensional representation. This explains why the E_g modes are usually in-plane vibrations; this is evident in the Raman tensor. Raman scattering is dependent on the polarization vectors of incident and scattered light. The polarization configuration is crossed polarized if the incident light is polarized perpendicular to the scattered light, while it is a parallel configuration if the direction of polarization is the same for both incident and scattered light. This dependence arises from the symmetry properties of the derivative of the polarizability tensor with respect to the vibrational coordinate of a normal mode. This derivative is referred to as the Raman tensor of the particular normal mode. The Raman tensors of these modes may be written as

$$A_{1g} = \begin{pmatrix} a & 0 & 0 \\ 0 & a & 0 \\ 0 & 0 & b \end{pmatrix} \qquad E_g = \begin{pmatrix} c & 0 & 0 \\ 0 & -c & d \\ 0 & d & 0 \end{pmatrix} \quad \text{or} \quad \begin{pmatrix} 0 & -c & -d \\ -c & 0 & 0 \\ -d & 0 & 0 \end{pmatrix}.$$

In the Raman tensor for the A_{1g} mode above, it is obvious that off diagonal elements are zero, this implies that the intensity of this mode in a cross polarization configuration is zero, invariably this mode will only be active for parallel polarization configuration. On the other hand, the E_g mode has non-zero off diagonal elements which implies that this mode is expected in a cross polarization configuration, its activity/presence in parallel configuration will depend on which of the matrices describes this mode, but in most cases, it is present in this configuration but with a reduced intensity. This piece of information will come handy in assigning the spectral peaks that appear in our Raman spectrum with vibrational modes.

Chapter 3

Experiment

3.1 Sample Preparation

3.1.1 Bi_2Se_3, Bi_2Te_3, and Sb_2Te_3

The Bi_2Se_3, Bi_2Te_3, and Sb_2Te_3 samples used in this study were provided by Takao Sasagawa of the Tokyo institute of Technology. Details of the fabrication process is described in [58]. A summary of this process is included here. Single crystals of Bi_2Se_3, Bi_2Te_3, and Sb_2Te_3 were grown by a modified Bridgman method in sealed evacuated quartz tubes. The starting materials used were high purity (99.999 %) chunks of bismuth, antimony, tellurium, selenium in stoichiometric ratios. During the sealing of the tube, one end of the quartz tube was carefully prepared in a conical shape for the starting point of the crystal growth. The mixture was allowed to melt completely at $T > 950°C$ in the sealed quartz tube, the tube was mechanically agitated to ensure a homogenous mixing of the constituents. The molten mixture was slowly cooled from the conical end of the tube, so that the nucleation of a single crystal grain starts

from there and propagates along the tube. Flakes of single crystal Bi_2Se_3, Bi_2Te_3, and Sb_2Te_3 of a couple of hundreds of microns thick were subsequently obtained.

3.1.2 WSe_2

The Single crystals of WSe_2 samples used in our experiments were provided by our collaborator Veerle Keppens of The University of Tennessee, Knoxville. In order to grow single crystals of WSe_2, the chemical vapour transport method was utilized with iodine as the transport agent. Powders of tungsten (99.999%) and selenium (99.999%) were mixed and ground inside a glove box. The powder mixture was then placed in a quartz tube at room temperature, the temperature was then increased to 100°C in 1.5 hours and allowed to dwell for 19 hours. The temperature was then increased to 200°C in 2 hours and allowed to dwell for 19 hours, after which it was increased to 400°C in 4 hours and allowed to dwell for 2 hours, and to 650°C in 5 hours and allowed to dwell at 650°C for 36 hours. Finally, the temperature was increased to 900°C in 12 hours and allowed to dwell for 7 days. Upon completion, the sample is furnace-cooled.

The resulting WSe_2 powder was resealed in a 17 mm inner-diameter quartz tube along with iodine in a 6:1 ratio. The tube was evacuated and backfilled with argon twice, and then evacuated a final time, sealed, and placed in a tube furnace. The furnace was heated to 1050°C at a rate of 1°C/minute and allowed to dwell for 10 days, after which single crystals were obtained.

3.2 Experimental setup

3.2.1 Raman Scattering

The Raman experiments were carried out in backscattering geometry using a Renishaw inVia Raman Microscope. Spectra were collected at room temperature in air. A schematic diagram of the optical system is shown in Figure 3.1. The light source was a diode laser with wavelength in the near infrared region (830 nm), the laser beam power was set to $\simeq$ 3 mW (approximately 10% of the maximum laser power). The light passes through a beam expander B, that expands the beam, after which it passes through a collection of mirrors and lenses M1 and M2. The vertically polarized light from the laser hits the sample (which sits on a microscope translation stage) through an optical microscope MS (allowing confocal measurements) that shines the light on the sample S and collects the scattered light. The holographic filter, F, allows for only a tiny fraction of the scattered light reaching it to pass, this fraction of light which is the Raman scattered light is then incident on a diffraction grating G, which splits it into component wavelengths. A CCD camera detects this light and outputs the resulting spectrum to a computer (not shown in the figure). The computer also serves as an interface to input parameters required to produce a desirable spectrum for each run of experiment. The set-up is equipped with a video camera from which images of the sample can be taken.

Figure 3.1: Schematics of Renishaw Invia Raman microscope. The red arrow head shows the path travelled by incident light from the laser while the green arrow head shows the path travelled by scattered light to the CCD detector. B - Beam expander, M1 - Mirror 1, M2 - Mirror 2, MS - Microscope, S - Sample, F - Holographic filter, G - Diffraction grating.

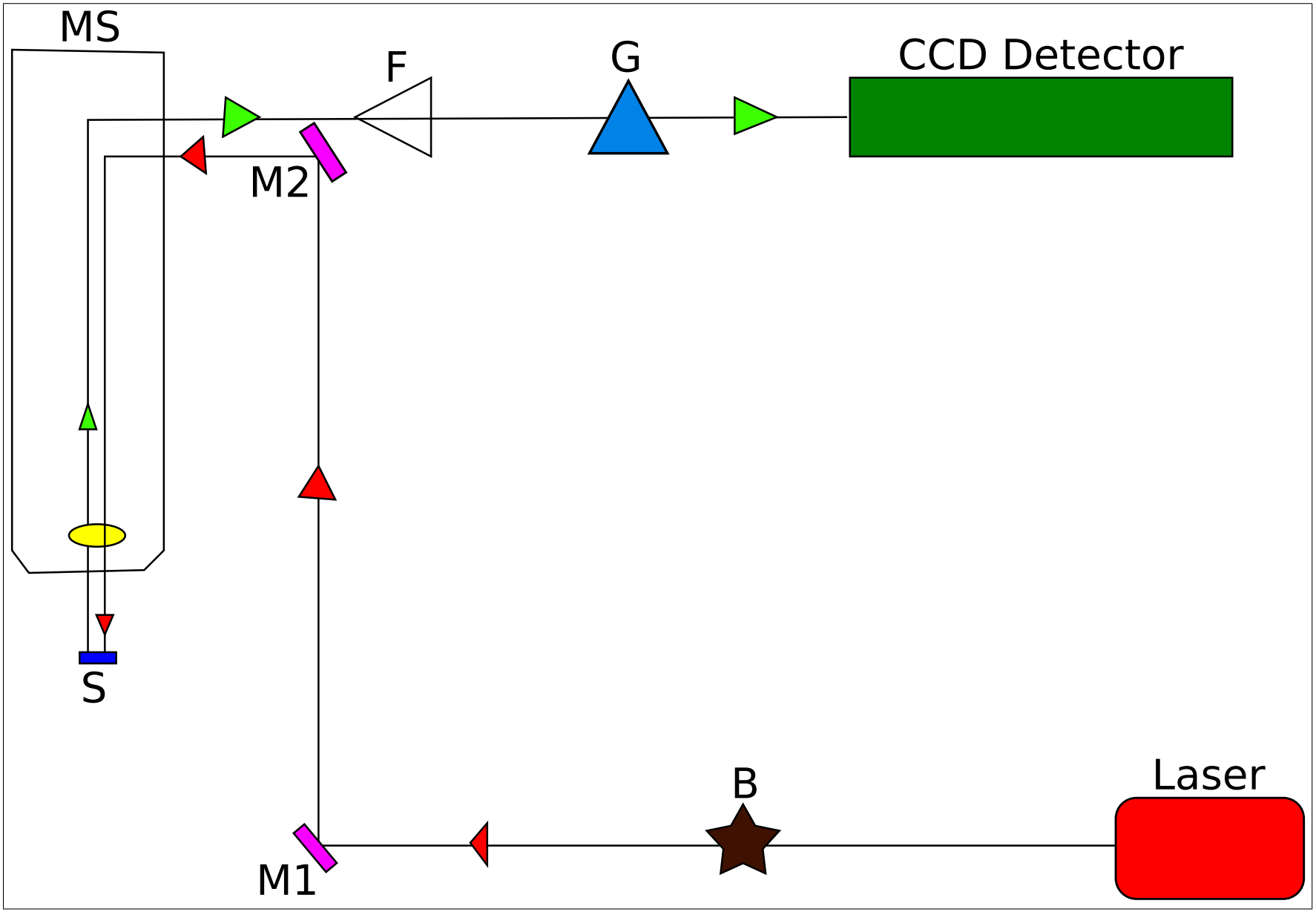

The Renishaw's Windows-based Environment (WiRE) software installed on the computer system allowed for setting parameters to produce a desirable spectrum. A brief description of some of these parameters that can be set/controlled is given in Table 3.1. More information about the WiRE software can be found in Ref. [59].

With the parameters in Table 3.1 set, the average time to collect a spectrum with a good signal-to-noise ratio was about 45 min. All spectra are reported with Raman shifts on the horizontal axis and intensity in arbitrary units on the vertical axis. The Raman shifts are reported in wavenumbers.

$$\bar{\nu} = \frac{1}{\lambda} = \frac{\nu}{c} \tag{3.1}$$

where $\bar{\nu}$ is the wavenumber in cm^{-1}, λ is the wavelength, ν is the frequency and c is the velocity of light. Basically, Raman shift is the difference in wave number between the exciting laser line and the observed lines appearing in a Raman spectrum. For instance, the 521 cm^{-1} Raman line of silicon implies that the Raman peak of silicon is 521 wavenumbers away from the exciting laser line. Before collecting our Raman spectra, we did a quick calibration run to ascertain that the silicon line was at 521 cm^{-1}. In the case where it was not, we added the difference into our reported Raman shift. Due to a filter in the optical system, Raman shifts less than or equal to 80 cm^{-1} were not observable. This filter was necessary so as to prevent saturating the detector with intense light when scanning towards the laser line at 0 cm^{-1}.

Table 3.1: Experimental parameters, description and corresponding values used in this work.

Parameter	Description	Set values
Objective	This indicates the magnification of the objective used, higher magnification objective gives better signal-to-noise ratio.	50x
Exposure time	The time the detector is exposed to the Raman signal. A longer exposure time produces a better signal-to-noise ratio.	600 s
Accumulations	The number of times a scan is repeated. When set to a value greater than one, spectrum are automatically co-added to produce spectra with better signal-noise ratio.	3−5
Cosmic ray removal	Removes random sharp peaks due to comic rays that might be present.	Yes

3.2.2 Brillouin Light Scattering

The experimental setup for the Brillouin scattering studies is shown in Figure 3.2. A solid state laser operating at a wavelength of 532 nm and a beam power of 60 mW served as the incident light source. The beam from the laser is made to pass through a beam splitter BS, where part of it is directed via a mirror M2 to the tandem Fabry-Perot interferometer TFP-1. This beam serves as a reference beam and is used to maintain alignment of the two interferometers in the TFP-1. The intensity of the reference beam is controlled by a variable neutral density filter. The less intense reference beam is used when scanning over the high intensity region of elastically scattered light in lieu of the scattered light from the sample which if used could cause a saturation of the detector, otherwise the reference beam is blocked and light from the sample allowed into TFP-1. The use of the reference beam for this purpose is made possible through the incorporation of a shutter system in the TFP-1 which prevents elastically scattered light from entering the interferometer and uses the less intense reference beam instead.

The beam that passes through the beam splitter has its path redirected 90° by a mirror M1. This beam goes through a filter VNDF1 whose purpose is to control the power of the beam reaching the sample surface, the beam then undergoes total internal reflection on the prism P, and is made to pass through a focusing lens with focal length 5 cm to the sample S. The focusing lens also serves as a collecting lens for the scattered light from S. The scattered light is then made to pass through another lens L of focal length 40 cm which brings the light to a focus on the input pinhole of the interferometer. The size of this pinhole can be adjusted. For the purpose of our

experiments it was set to 300 μm. The scattered light finally finds its way into the tandem Fabry-Pérot interferometer TFP-1 where it is frequency analyzed.

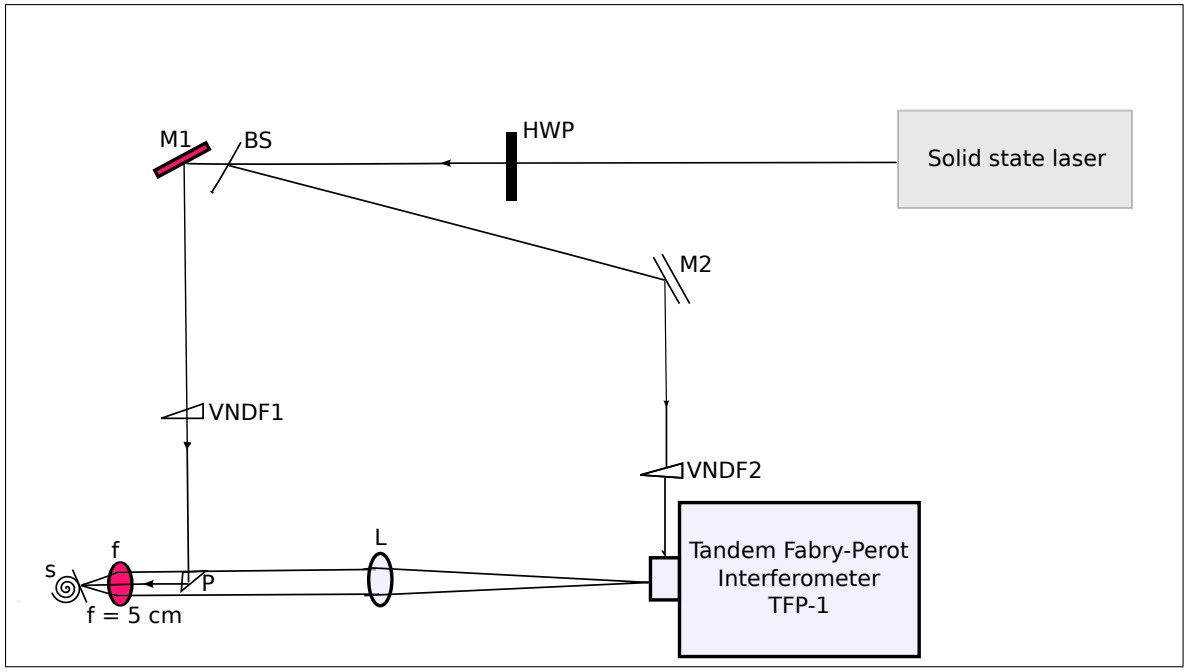

Figure 3.2: Schematic of the Brillouin light scattering set-up. HWP - half wave plate, BS - beam splitter, M - mirror, VNDF - variable neutral density filter, L - lens, P - prism, f - focusing/collecting lens.

The TFP-1 consists of two Fabry-Pérot etalons/interferometers (FP), each of which consists of two plane mirrors mounted parallel to one another, with a spacing L_i between them ($i = 1$ or 2) [60]. The condition

$$L_i = \frac{1}{2} m\lambda \tag{3.2}$$

has to be fulfilled for a wavelength to be transmitted by the individual FP, where m can be any integer. The above condition is the resonance condition of the FP interferometer. The wavelength (frequency) difference of two consecutive resonances

(transmission maxima) is referred to as the free spectral range (FSR). The FSR is usually reported in units of frequency and can be calculated by using $\nu = \frac{c}{\lambda}$ and the expression for λ from equation (3.2) for $m = 1$. FSR can thus be expressed in terms of the mirror spacing as [61]

$$\nu_{FSR} = \frac{c}{2L_i}. \tag{3.3}$$

The FSR is typically chosen to include the range of frequency where the acoustic phonons appear. In the current work, our Brillouin shifts appeared at frequencies < 15 GHz, and thus our choice of 20 GHz FSR.

The width $\delta\nu$ of a given transmission maximum is related to the FSR through a property known as the finesse, F of the FP, given as

$$F = \frac{\Delta\nu}{\delta\nu}. \tag{3.4}$$

The finesse is primarily dependent on the reflectivity and flatness of the Fabry-Pérot mirrors. In principle, F cannot be made much greater than 100 due to limitations on the quality of mirrors. The higher the finesse, the better the resolution of the TFP-1. Finesse in the present work is $\simeq 100$.

The use of a tandem Fabry-Pérot interferometer has the advantage of increased FSR at a fixed resolution. The two FPs are placed in series arrangement with the spacing of the second interferometer L_2 close to that of the first L_1.

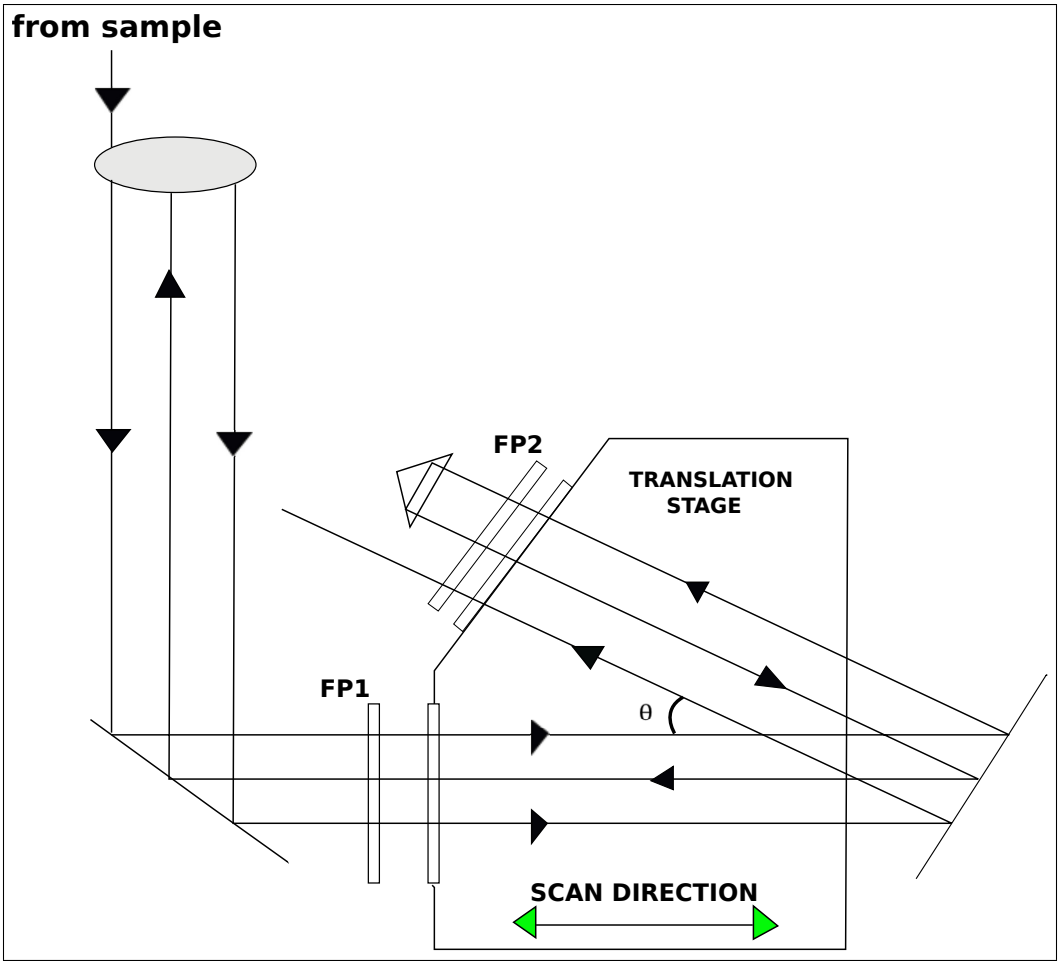

Figure 3.3: Tandem Fabry-Pérot Interferometer showing 3+3 pass.

Figure 3.3 shows the arrangement of both interferometers. The first interferometer FP1 has its normal in the direction of the translation stage movement, while the second interferometer FP2 has its normal at an angle θ to the scan direction. In both interferometers, one mirror sits on the translation stage while the other mirror is on a separate orientation device which allows for slight adjustment be made to the mirror spacing. The translation stage is mounted in such a way that for a movement either to left or right, the mirror spacing in both interferometers are related by $L_2 = L_1 \cos\theta$.

A movement of the translation stage that produces a change δL_1 in L_1 produces a corresponding change $\delta L_2 = \delta L_1 \cos\theta$ in L_2. In order to scan a given increment in wavelength, such changes δL_1 and δL_2 must satisfy [62]

$$\frac{\delta L_2}{\delta L_1} = \frac{L_1}{L_2}. \tag{3.5}$$

In the JRS instruments tandem interferometer employed for the present measurements, a 3+3 pass arrangement is used (as shown in Figure 3.3) in which light passes through each of the two FPs three times in order to improve the contrast before being transmitted to the photodetector. An external control unit stabilizes the TFP-1, while a vibration isolation control unit is used to cushion the effect of any other vibrations that might disrupt the alignment of the TFP-1 optics. The counted phonons are displayed via *Ghost* [63] software on a computing screen where it is viewed as a spectrum.

Chapter 4

Results and Discussion

The results of Raman scattering studies of Bi_2Se_3, Bi_2Te_3, Sb_2Te_3, and WSe_2 as well as Brillouin light scattering studies of WSe_2 are presented. All studies were carried out in air at room temperature.

In all of the Raman spectra presented in this thesis, the Raman shift (in cm^{-1}) is shown on the horizontal axis while intensity (in arbitrary units) is plotted on the vertical axis. Unpolarized Raman spectra showed a better signal-to-noise compared to polarized spectra. The polarization studies carried out will be reported using the Porto notation. The Porto notation is a way of expressing the orientation of the crystal with reference to the polarization of the laser in both the excitation (incident) and analyzing (scattering) directions. This notation consists of a four-letter code (a combination of the three coordinate axes) expressing the scattering geometry where the letters indicate the direction of the propagation of the incident radiation, the polarization of the incident radiation, the polarization of the scattered radiation, and the direction of propagation of the scattered radiation. For example, in the code

$z(xy)\bar{z}$, z is the axis for the propagation of the laser light, x is the orientation of the polarization direction *i.e.* the direction of polarization of the incident light from laser with respect to the sample's plane of incidence, y is the vibrational direction of the Raman scattered photons that are being analyzed and $\bar{z}$ is the direction of propagation of the analyzed laser beam. This example is in a backscattering geometry, due to the presence of z and $\bar{z}$ surrounding the parentheses. Due to the fact that all of our Raman spectra were collected in the backscattering geometry, we drop the first and last letters of the Porto notation. Unless otherwise stated, Raman spectra were collected within the frequency range $100-300$ cm^{-1}, which was necessary as the filter in our Raman set-up cuts off low frequency shift peaks ($<$ 100 cm^{-1}).

4.1 Raman Scattering of Topological insulators

4.1.1 Bi_2Se_3

Raman spectra of Bi_2Se_3 showed two strong peaks in the frequency range studied. Evidence supports that there exists two other peaks appearing at low frequencies inaccessible to our Raman set-up hence they were not observed in our spectra [21]. The unpolarized Raman spectrum shown in Figure 4.1 shows the two peaks, one at 132 cm^{-1} and the other at 174 cm^{-1}, with the intensity of the former greater than the latter. To assign our observed peaks to particular vibrational modes, polarization studies were carried out and the resulting spectra were interpreted using group theory analysis.

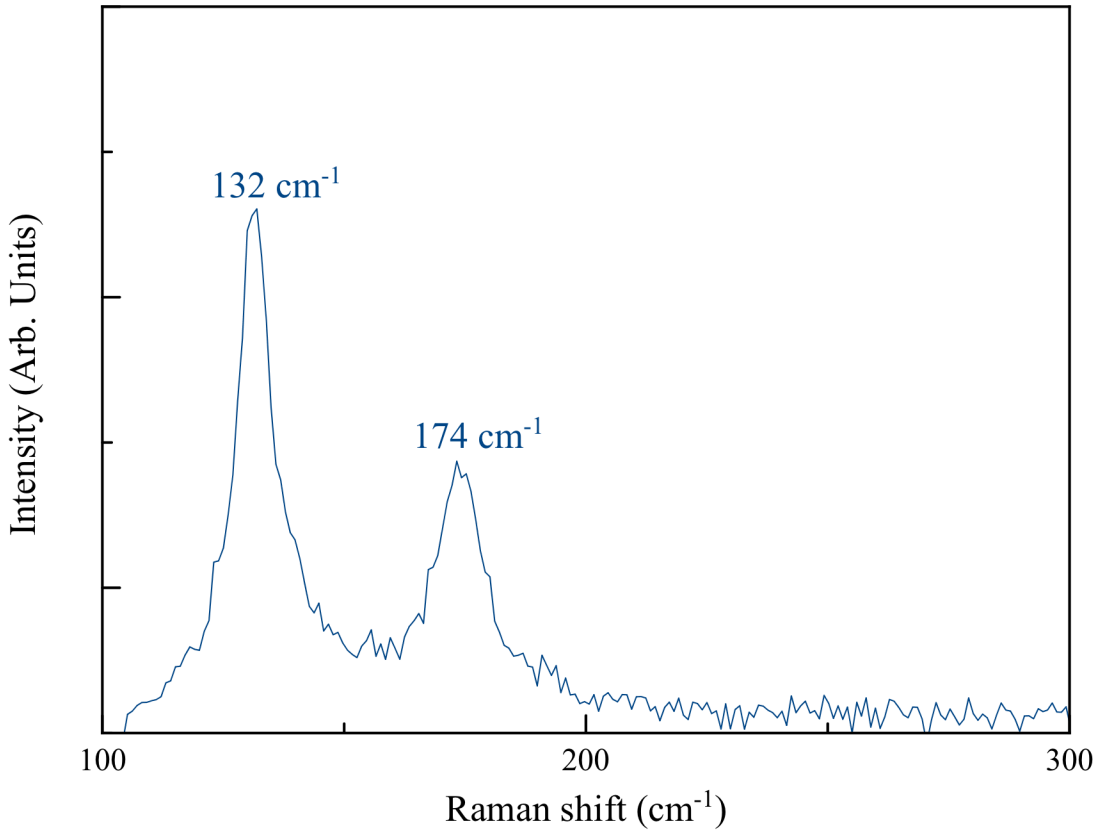

Figure 4.1: Unpolarized Raman spectrum of Bi_2Se_3.

Figure 4.2 shows the polarization results for Bi_2Se_3. Using the Porto notation, in the (xy) spectra of Bi_2Se_3, we see that the peak at 174 cm^{-1} totally disappears. Using knowledge of how the Raman tensor described in Section 2.3.3 transforms, we deduce that the peak at 132 cm^{-1} is due to an E_g mode (since the xy configuration implies non-zero off-diagonal elements). To verify the origin of the peak at 174 cm^{-1} which disappeared in the (xy) spectra, we collected a spectrum with (xx) polarization.

The signal-to-noise ratio in the (xx) spectrum is low, but high enough to identify the two peaks as seen in Figure 4.2. The just assigned E_g is at 132 cm^{-1}. The other is assigned as an A_{1g} mode, since it appeared in (xx) polarization configuration but did not in the (xy) configuration. The label for these modes, their frequency shifts in wave numbers and results obtained by other authors [21, 25, 35, 36] are shown in Table 4.1. The superscript (2) attached to both modes is used to signify that there exists a mode with the same symmetry but appearing at a lower wavenumber which is inaccessible to our detector as previously stated. This is further confirmed by results of previous studies [21].

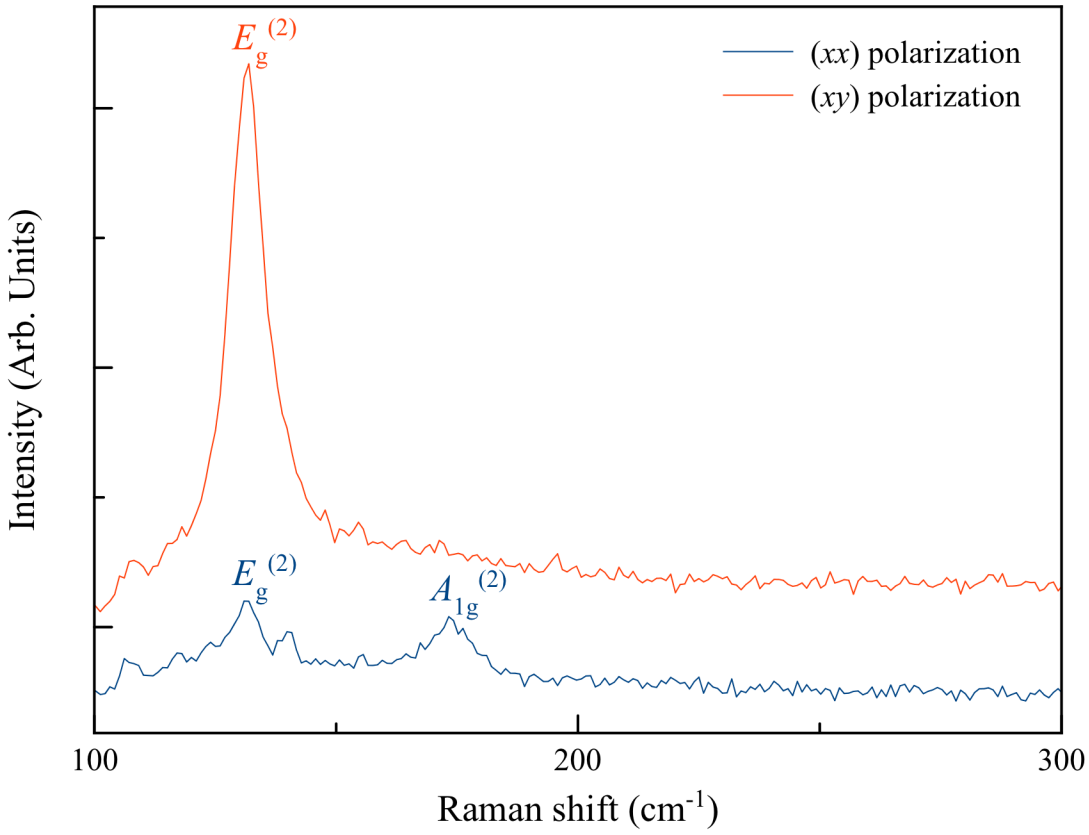

Figure 4.2: Polarized Raman spectrum of Bi_2Se_3.

Table 4.1: Raman active modes in Bi_2Se_3 and Raman Shifts.

	Raman Shift (cm^{-1})				
	This Work]	[21]	[25]	[35]	[36]
$E_g^{(2)}$	132 ± 1	131.5	131	130	131.5
$A_{1g}^{(2)}$	174 ± 1	174.5	174	173	175.5

We further exfoliated our Bi_2Se_3 sample to see what effect this has on the position and intensity of the spectral peaks. Mechanical exfoliation was done using a two-sided Scotch tape. Resulting exfoliated samples were considerably thinner than what they were before the exfoliation process. We managed to exfoliate the original sample into about 3 thinner samples. Figure 4.3 shows spectra of exfoliated and non-exfoliated samples. The peak positions were the same as those obtained before sample was exfoliated.

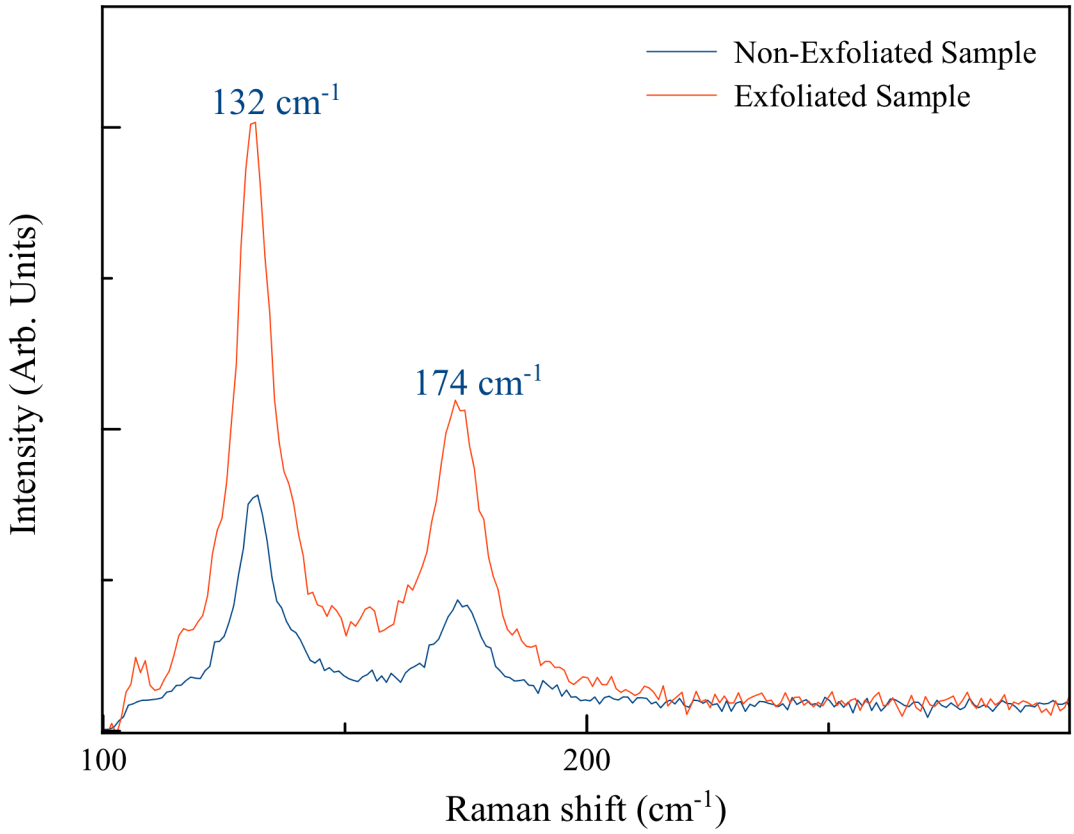

Figure 4.3: Raman spectra of exfoliated and non-exfoliated Bi_2Se_3.

4.1.2 Bi_2Te_3

Contrary to the four spectral peaks predicted by group theory, unpolarized Raman spectrum of Bi_2Te_3 reveals two spectral peaks, similar to what was observed in Bi_2Se_3 but at lower shifts: 104 cm^{-1} and 136 cm^{-1}. We hypothesize that the other two peaks are not observable in our spectrum due to their low Raman shifts, in this case < 100 cm^{-1}. The observed peaks are shown in Figure 4.4. The peak at 136 cm^{-1} obviously has a greater intensity compared to that at 104 cm^{-1}.

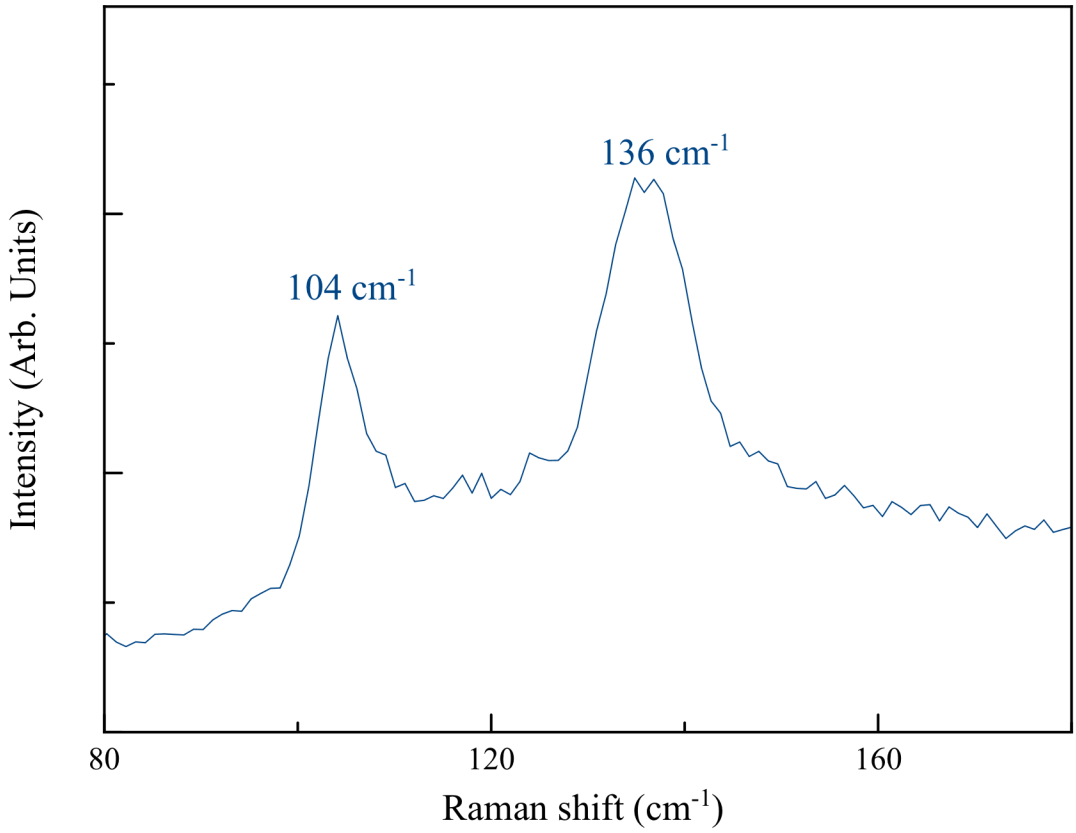

Figure 4.4: Unpolarized Raman spectrum of Bi_2Te_3.

We conducted polarization studies to study the nature of spectral peaks observed and classify them accordingly. In the (xy) spectra, only one peak was observed at 104 cm^{-1} and using the argument presented for how the modes behave under this polarization configuration, we assigned this peak as due to an E_g mode. In the (xx) spectra, two peaks were observed. We assigned the peak at 136 cm^{-1} as due to an A_{1g} mode. The labels of the assigned modes, and their Raman shifts are presented in Table 4.2, which also contains results reported by other authors [18, 21, 29, 64].

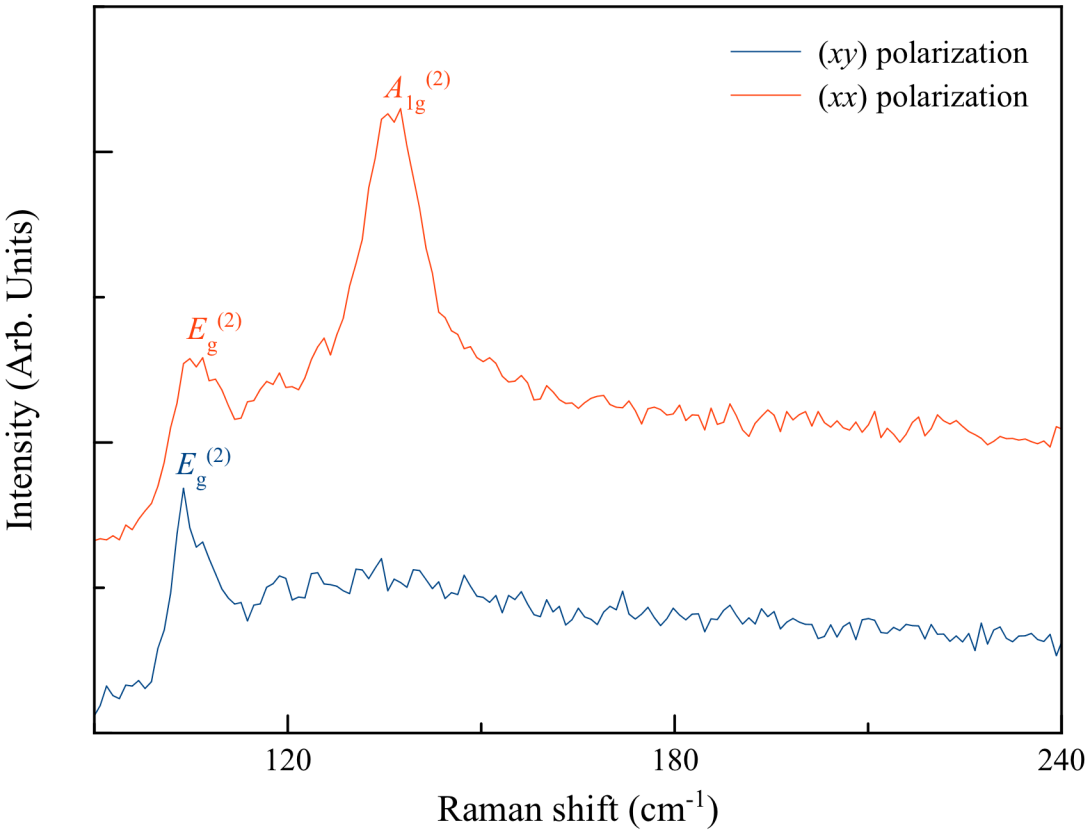

Figure 4.5: Polarized Raman spectrum of Bi_2Te_3.

We compared our unpolarized spectrum with that reported by Shahil *et. al.* [18]. One notable difference was in the relative intensities of the two modes. From our unpolarized spectra, the peak due to the $A_{1g}^{(2)}$ mode is more intense than that due to the $E_g^{(2)}$ mode. Shahil *et. al.* [18] argued that in bulk Bi_2Te_3, the peak associated with the $E_g^{(2)}$ mode has a greater intensity than that associated the $A_{1g}^{(2)}$ mode, with the latter increasing in intensity as sample thickness goes to a few nanometers. In this regard, their argument is inconsistent with our observation, as we observed that the peak due to the $A_{1g}^{(2)}$ mode is greater in intensity than that of the $E_g^{(2)}$ mode in bulk samples of Bi_2Te_3. We should mention that both studies were done using different laser excitation energies, so that this might point to the presence of some resonance effects at play.

Table 4.2: Raman active modes in Bi_2Te_3 and Raman Shifts.

	Raman shift (cm^{-1})				
	[This Work]	[18]	[21]	[29]	[64]
$E_g^{(2)}$	104 ± 1	101.7	103	104	102.3
$A_{1g}^{(2)}$	136 ± 1	134	134	137	134

In order to ascertain what effect a significant reduction in sample thickness has on the observed spectral peaks, Raman spectra of mechanical exfoliated samples were collected. We proceeded with the exfoliation as described for Bi_2Se_3. comparison of the resulting spectra to the non-exfoliated spectra in Figure 4.6 shows that the

position of observed spectral peaks remained approximately the same. The relative intensities of the peaks did change. Apparently, a similar trend was observed in the Raman spectra of few quintuple layered samples.

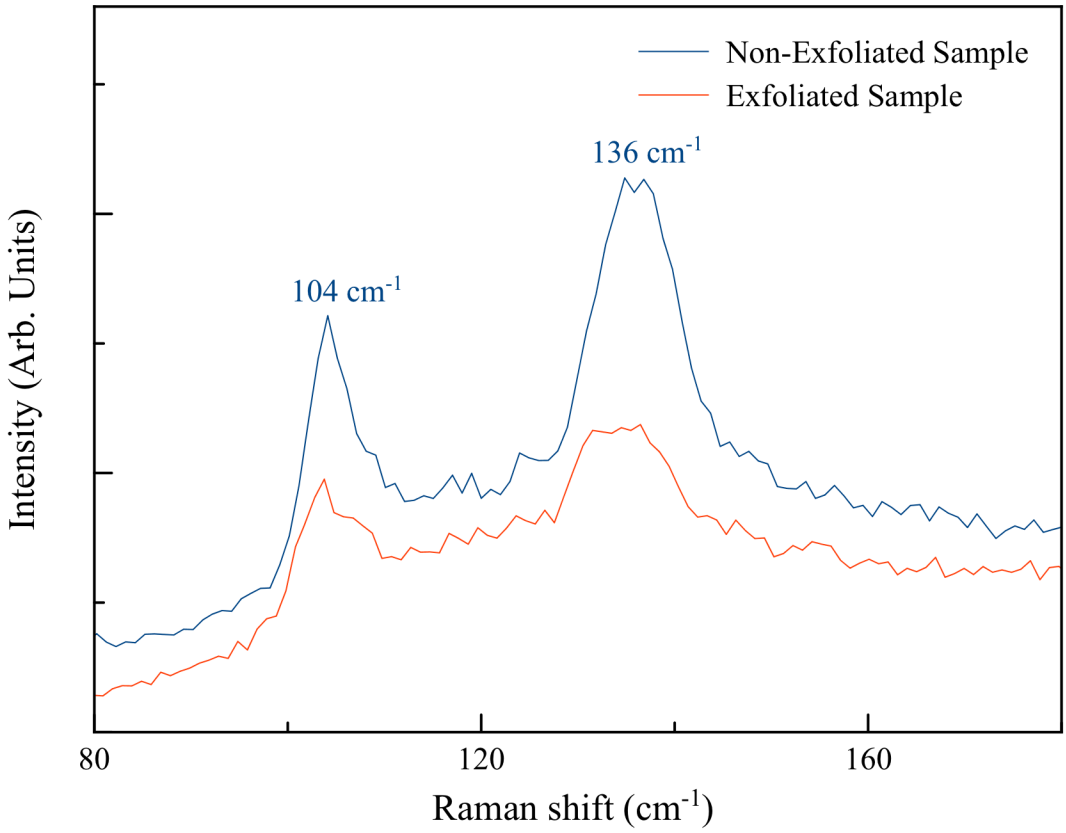

Figure 4.6: Raman spectra of exfoliated and non-exfoliated Bi_2Te_3.

4.1.2.1 Sb_2Te_3

A similar trend to Bi_2Se_3 and Bi_2Te_3 was observed in the Raman spectrum of Sb_2Te_3. Figure 4.7 shows the unpolarized Raman spectrum of bulk Sb_2Te_3. Two spectral peaks with Raman shifts 114 cm^{-1} and 167 cm^{-1} were observed. The other

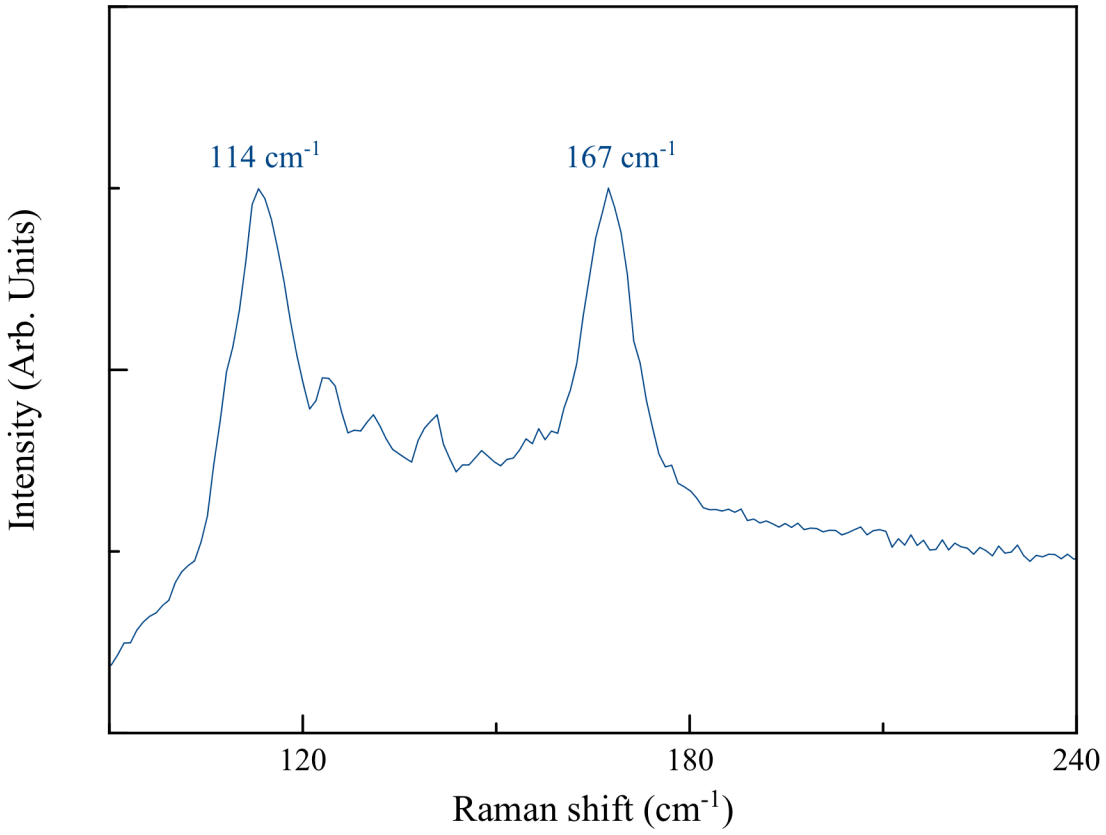

Figure 4.7: Unpolarized Raman spectrum of Sb_2Te_3.

two expected Raman peaks predicted by theory were not observed due to the filter in our Raman set-up. The tiny peak-like signatures observed between 120 cm^{-1} and 150 cm^{-1} have been verified to be an effect from the laser, and not from the sample, and can therefore be ignored in all spectra.

We carried out polarization studies to correctly assign these spectral peaks to particular vibrational modes by obtaining (xy) and (xx) polarized spectra (shown in Figure 4.8). In the (xy) spectrum of Sb_2Te_3, we observed a single peak at 114 cm^{-1}, which we assigned as originating from an $E_g^{(2)}$ mode (as discussed for the cases

of Bi_2Se_3, and Bi_2Te_3), while in the (xx) spectrum two peaks were observed. We assigned the other spectral peak at 167 cm^{-1} as originating from an $A_{1g}^{(2)}$ mode. As expected, the intensity of the peak due to the $E_g^{(2)}$ mode is reduced but not to zero, in the (xx) polarization spectrum.

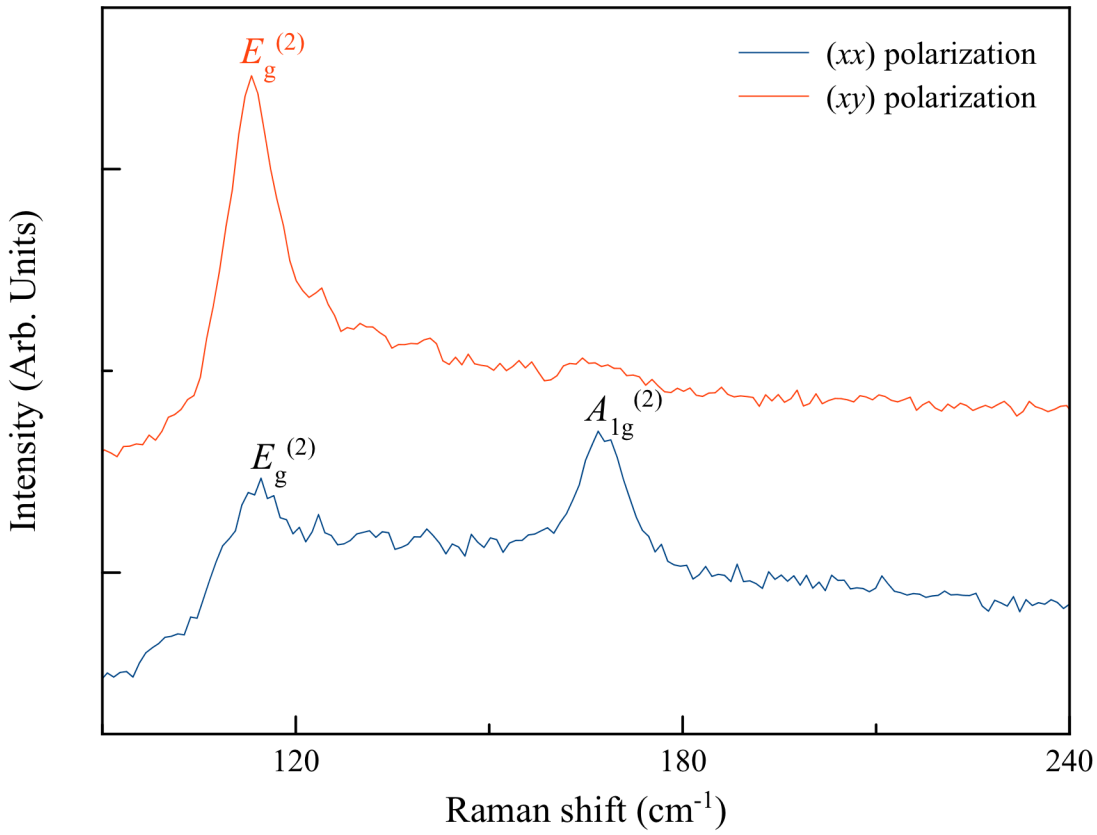

Figure 4.8: Polarized Raman spectrum of Sb_2Te_3.

Table 4.3 shows the observed vibrational mode assignments, the Raman shifts of the associated spectral peaks and those of other authors [19, 21, 36, 65]. Results reported by Shahil *et al.* [18] are consistent with our observation in terms of the

Table 4.3: Raman active modes in Sb_2Te_3 and Raman Shifts.

	Raman Shift (cm^{-1})				
	[This Work]	[19]	[21]	[36]	[65]
$E_g^{(2)}$	114 ± 1	114.5	112	-	110
$A_{1g}^{(2)}$	167 ± 1	167.5	165	168.8	165

Raman shift. The difference that stands out between their report and ours is in the intensities of observed modes. They reported that the peak due to the $E_g^{(2)}$ mode has a higher intensity than that due to the $A_{1g}^{(2)}$ mode, which contradicts our observation that this intensity ratio is $\simeq 1$. Again this might be as a result of the difference in laser excitation energies.

Similar to what we observed for exfoliated samples of Bi_2Se_3 and Bi_2Te_3, exfoliated samples of Sb_2Te_3 showed no difference in peak positions and relative intensity when compared to that before sample was exfoliated. Figure 4.9 shows how the spectra of exfoliated samples compares to that of non-exfoliated samples.

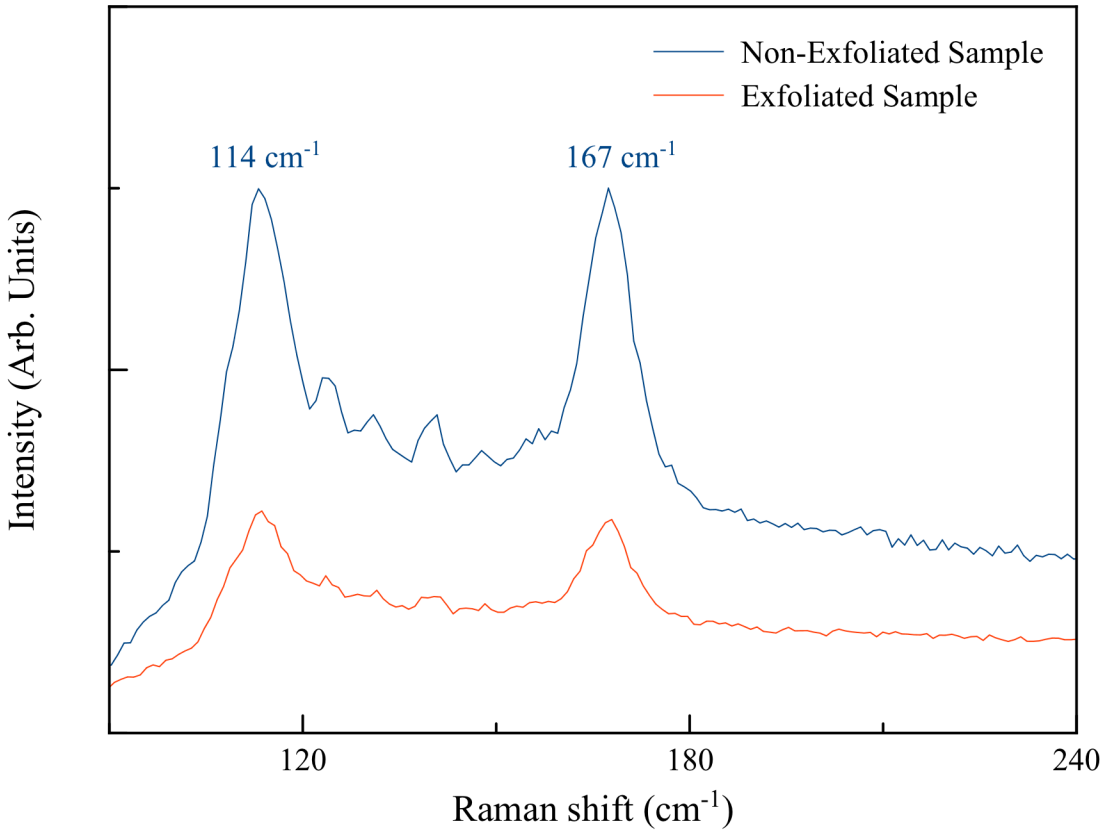

Figure 4.9: Raman spectra of exfoliated and non-exfoliated Sb_2Te_3.

4.1.3 Discussion

In the case of the topological insulators studied in this work, we verified the validity our mode assignment by results of polarization experiments. In general, the Raman shift reported by other authors agreed with ours within 2 cm^{-1}, as can be seen from the Tables 4.1, 4.2, 4.3.

Only two spectral speaks were observed in our Raman spectra across all three samples. We expect that the other two peaks resulting from the remaining two

vibrational modes ($E_g^{(1)}$ and $A_{1g}^{(1)}$) predicted by group theory appear at Raman shift below the threshold of what is observable in this experiment. This expectation is supported by considering the argument raised by Shahil *et al.* [19] that the $E_g^{(1)}$ and $A_{1g}^{(1)}$ modes occur at lower frequencies than the $E_g^{(2)}$ and $A_{1g}^{(2)}$ modes as a result of the nearest neighbour distance values. Table 4.4 shows the nearest neighbour distance for all three samples.

Table 4.4: Nearest-neighbour distances in Bi_2Te_3, Sb_2Te_3 and Bi_2Se_3 [66].

	Nearest neighbour atoms [distance (nm)]		
Bi_2Te_3	$Bi-Te^{(1)}$ [0.304]	$Bi-Te^{(2)}$ [0.324]	$Te^{(1)}-Te^{(1)}$ [0.372]
Sb_2Te_3	$Sb-Te^{(1)}$ [0.306]	$Sb-Te^{(2)}$ [0.316]	$Te^{(1)}-Te^{(1)}$ [0.364]
Bi_2Se_3	$Bi-Se^{(1)}$ [0.299]	$Bi-Se^{(2)}$ [0.307]	$Se^{(1)}-Se^{(1)}$ [0.330]

Shahil *et al.* [19] argued that the movement of the $Bi-Te^{(1)}$, $Sb-Te^{(1)}$, $Bi-Se^{(1)}$ atoms is responsible for the $E_{1g}^{(1)}$ and $A_{1g}^{(1)}$ modes while the movement of the $Bi-Te^{(2)}$, $Sb-Te^{(2)}$, $Bi-Se^{(2)}$ atoms is responsible for the $E_g^{(2)}$ and $A_{1g}^{(2)}$ modes in Bi_2Te_3, Sb_2Te_3, Bi_2Se_3 respectively. And since the nearest neighbour distance in the former are smaller than those of the latter, the $E_g^{(1)}$ and $A_{1g}^{(1)}$ occurs at lower Raman shift compared to the $E_g^{(2)}$ and $A_{1g}^{(2)}$ modes, supporting our expectation.

From our observations of the Raman shifts of the vibrational modes in all the three materials (Bi_2Se_3, Bi_2Te_3, Sb_2Te_3), we noted that the $E_g^{(2)}$ was consistently lower in shift than the $A_{1g}^{(2)}$ mode. Table 4.5 shows the frequency shifts for both the

$E_g^{(2)}$ and $A_{1g}^{(2)}$ mode and the peak intensity ratio ($I_{E_g^{(2)}}/I_{A_{1g}^{(2)}}$) for each of the three samples studied. The Raman bands in Bi_2Te_3 have the least Raman shift followed by those in Sb_2Te_3, and then Bi_2Se_3. This has been attributed to the strength of the bonding forces in these materials with the bonding force strongest in Bi_2Se_3 [19].

Table 4.5: Comparison of Raman shift of peaks due to $E_g^{(2)}$ and $A_{1g}^{(2)}$ modes and the peak intensity ratio for Bi_2Te_3, Sb_2Te_3 and Bi_2Se_3

	$E_g^{(2)}$ (cm^{-1})	$A_{1g}^{(2)}$ (cm^{-1})	$I_{E_g^{(2)}}/I_{A_{1g}^{(2)}}$ ($\pm$ 1)
Bi_2Te_3	104	136	0.9
Sb_2Te_3	114	167	1.0
Bi_2Se_3	132	174	1.3

Since all three materials have the same Wyckoff positions and crystal structure, it might be expected that there should be a uniform trend in the intensity ratio of the peak due to the $E_g^{(2)}$ mode to the $A_{1g}^{(2)}$ mode. It was however observed that this ratio is smallest in Bi_2Te_3, followed by Sb_2Te_3 and greatest in Bi_2Se_3 as shown in Table 4.5. This trend is likely due to the laser excitation wavelength used in this study 830 nm (1.49 eV). This most probably induced some resonance effect in Bi_2Te_3 and Sb_2Te_3 making the $A_{1g}^{(2)}$ mode in Bi_2Te_3 and Sb_2Te_3 gain intensity considerably, more than in Bi_2Se_3. A careful study of the electronic structure of these materials can be used to ascertain this. A similar trend has been reported in [19] where the authors found that by simply changing the laser excitation from 488 nm to 633 nm, there

was a huge increase in the intensity of the $A_{1g}^{(2)}$ mode with no observation of the $E_g^{(2)}$ mode under the resonant condition, whereas the $E_{1g}^{(2)}$ mode was the dominant feature in the spectrum collected under the 488 nm laser excitation wavelength.

Raman scattering studies of bulk Bi_2Se_3 reported by Ritcher *et al.* [21], their $E_g^{(2)}$ and $A_{1g}^{(2)}$ modes appeared 0.5 cm^{-1} away from what we reported, making their result in fair agreement with ours. It is worth mentioning that in their unpolarized spectrum, the intensity of the $E_g^{(2)}$ mode is approximately twice that of the $A_{1g}^{(2)}$ mode, agreeing with what we obtained. In the same vein, the result of the Raman shifts of the vibrational modes in Bi_2Te_3 and Sb_2Te_3 reported by Ritcher *et al.* [21] agrees within 2 cm^{-1} with those reported in the present work. The Raman shift of few-quintuple layer samples reported by Shahil *et al.* [18] for all three samples also agrees well with our results (within 2 cm^{-1} for the observed modes). Likewise the results reported in references [19, 25, 29, 35, 36, 64] are all in good agreement with those obtained here in terms of the reported shift. The only obvious difference is in the intensity of modes, which as earlier stated could be as a result of different laser excitation wavelength used in probing the samples.

4.2 Raman Scattering Studies of WSe_2

A number of second-order Raman modes alongside group theory predicted first-order Raman modes are expected in the Raman spectrum of the 2D semiconductor WSe_2. This has been verified in the Raman spectrum of materials with the Wurtzite structure [67]. In our unpolarized Raman spectrum of 2H-WSe_2, shown in Figure 4.10, we observed one very strong peak at 259 cm^{-1}, two moderately intense spectral

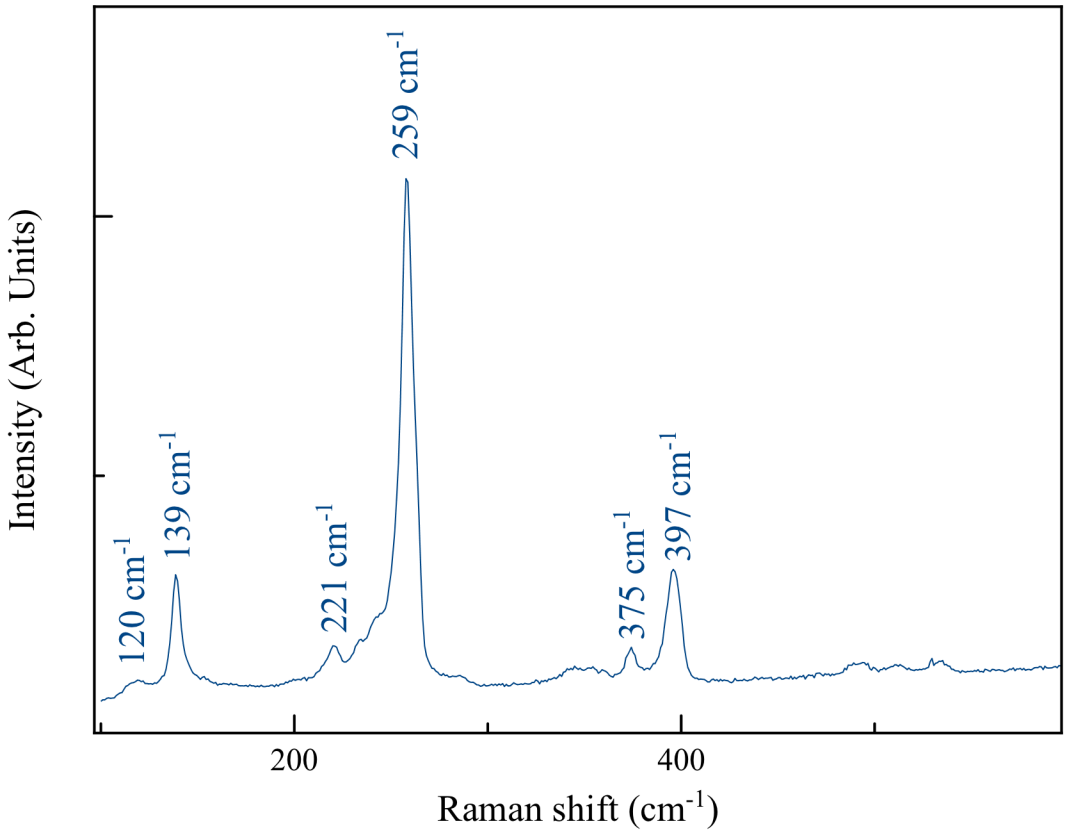

Figure 4.10: Unpolarized Raman spectrum of WSe_2.

peaks at 139 cm^{-1} and 397 cm^{-1}, and some smaller peaks at 120 cm^{-1}, 221 cm^{-1}, 375 cm^{-1}. There were also at least three peaks in the frequency region 490 cm^{-1} to 535 cm^{-1} which were later ascertained to be due to the laser. This was confirmed by obtaining Raman spectra of a piece of cardboard. These peaks were present in the spectrum obtained.

We employed polarization studies to enable us to assign the listed spectral peaks to specific vibrational modes. The scale of the (xx) polarization spectrum is three times that of the (xy) polarization spectrum. In the (xy) polarization configuration

shown in Figure 4.12, the spectrum showed no difference when compared to the unpolarized spectrum; all of the peaks still appeared at the same Raman shifts. In the spectrum of the (xx) polarization configuration shown in Figure 4.11, we observed three well separated peaks in the region 230 cm^{-1} to 259 cm^{-1}, contrary to what we observed in both the unpolarized and (xy) spectra. Another observation in the (xx) polarization setup was that the intensity of the peak at 259 cm^{-1} had reduced to about one-third compared to its intensity in the unpolarized spectrum. The spectral peak at 259 cm^{-1} happened to be the only peak that changed with respect to this polarization configuration; the other observed peaks showed unnoticeable or no variation in intensity and shift in this polarization configuration.

In the explanation of the Raman tensors presented in Section 2.3.3, in the (xy) polarization configuration we expect that an A_{1g} mode will vanish, since the off-diagonal elements of its Raman tensor are zero while an $E_{2g}^{(1)}$ mode, whose Raman tensor has non-zero off-diagonal elements, will be preserved/enhanced. We employ this idea in interpreting our polarized spectra. Since there was a splitting of the peak at 259 cm^{-1} in the (xy) polarization configuration with the overall intensity greatly reduced compared to what it was in the unpolarized spectrum, we conclude that the $E_{2g}^{(1)}$ mode has the lower contribution to the peak at 259 cm^{-1} compared to the contribution from the A_{1g} mode. We assigned the smaller peak at 249 cm^{-1} as originating from an $E_{2g}^{(1)}$ mode, and the peak at 258 cm^{-1} as due to an A_{1g} mode.

Two of the expected Raman active modes were not observed in our spectra, the $E_{2g}^{(2)}$ mode, likely due to its occurrence at a low energy (< 100 cm^{-1}), and the E_{1g} mode which is forbidden in backscattering geometry (see Ref. [41]).

Figure 4.11: Raman spectrum of WSe_2 in (xx) polarization configuration.

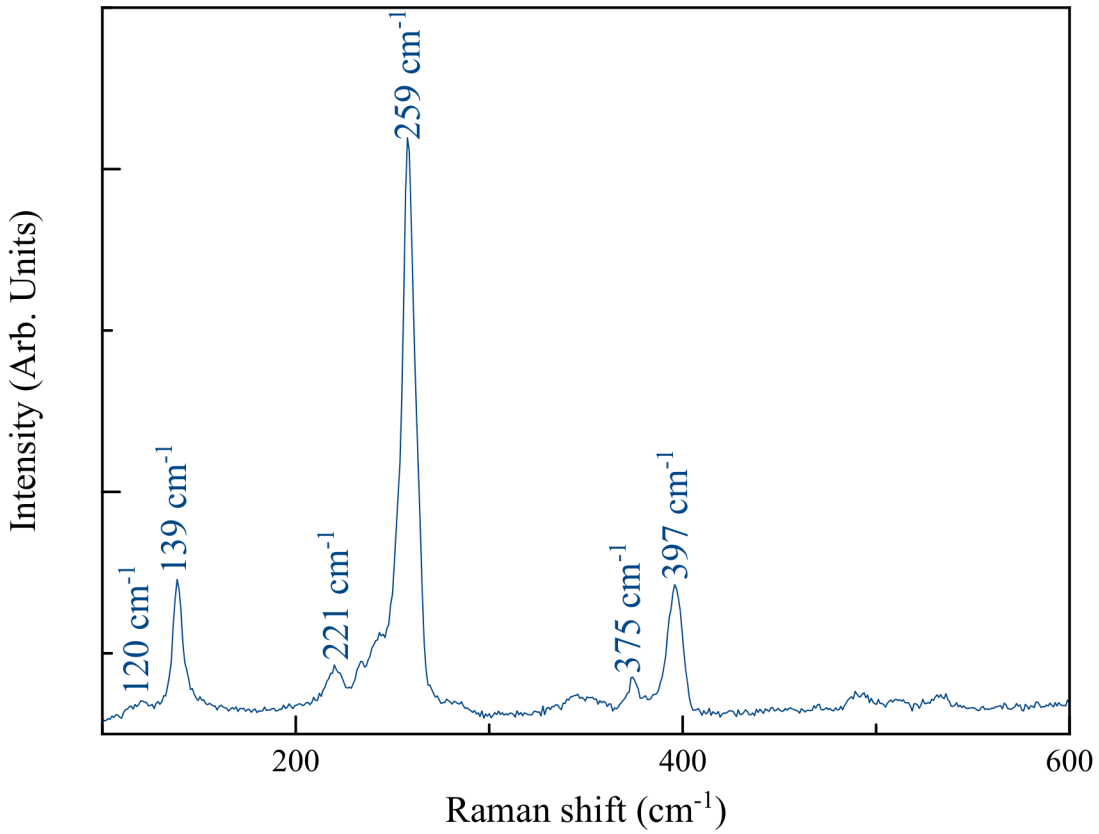

Figure 4.12: Raman spectrum of WSe_2 in (xy) polarization configuration. Note the splitting of the peak at 259 cm^{-1} (x3 magnification).

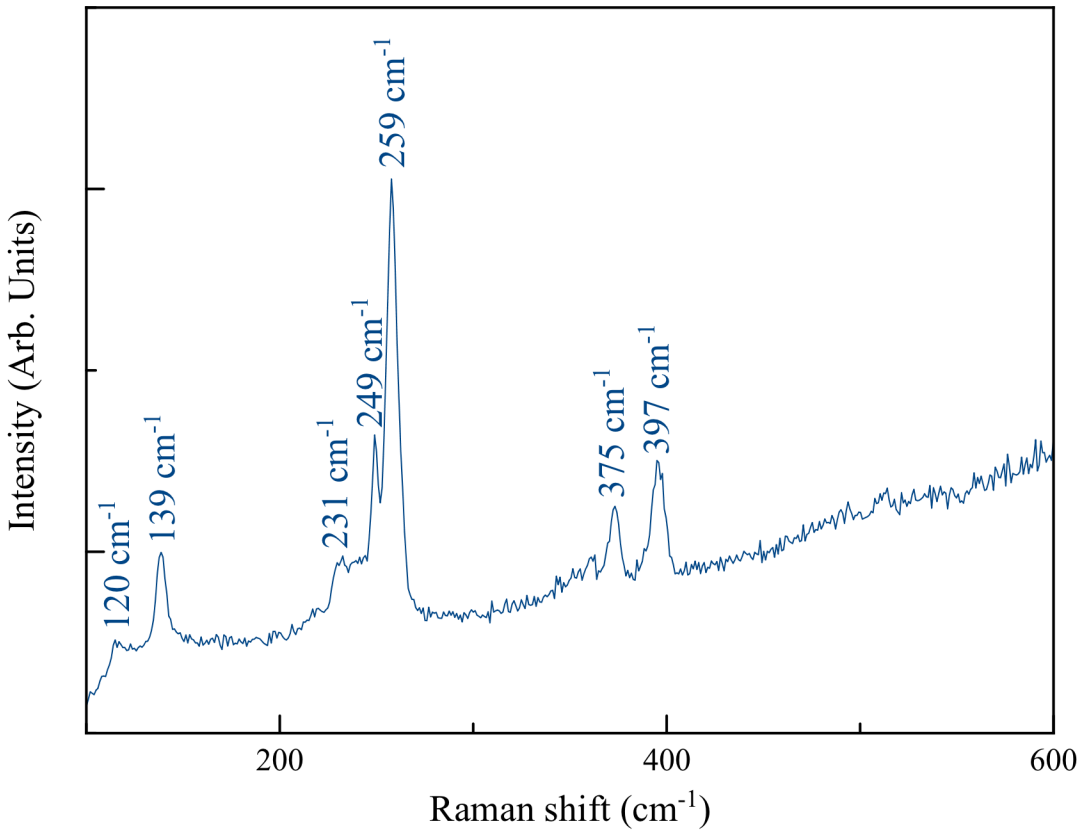

As earlier stated, the other peaks observed in the spectrum showed little polarization dependence, which is characteristic of vibrational modes originating from multi-phonon processes. Multi-phonon processes gives rise to second-order Raman modes, and unlike their first-order counterparts, are polarization independent.

Second-order Raman modes are expected to be present in the Raman spectra of 2H-WSe_2 owing to its polymorphic structure, as has been reported for materials with related structure (e.g, SiC [68], 2H-WS_2 [69]). These second-order Raman modes can either be multiples (e.g. $2A_{1g}$) or combinations (e.g. $A_{1g} + LA$) of pre-existing vibrational modes. Some of the second-order Raman modes observed in our experiment have frequencies corresponding to those previously reported in literature, however, we have observed at least two new ones that have not been previously reported. Table 4.6 shows a list of the observed peaks, mode assignments and Raman shifts.

Table 4.6: Raman shift and mode assignment in WSe_2. LA is a longitudinal acoustic mode, X_1 and X_2 signifies the two yet to be labelled second-order Raman modes we have observed.

	Raman Shift (cm^{-1})							
	LA	$A_{1g}-LA$	X_1	X_2	$E^{(1)}_{2g}$	A_{1g}	$A_{1g}+LA$	$2A_{1g}-LA$
[This Work]	120	139	221	231	249	259	375	397
[24]	–	136	–	–	–	–	–	–
[70]	121.4	137.4	–	–	247.1	256.5	371.6	393.3

4.2.1 Discussion

In the results of our Raman scattering studies of 2H-WSe_2, the prominent peak at 259 cm^{-1} in the unpolarized Raman spectra of WSe_2 has been determined to be span across at least three other peaks. On carrying out polarization studies, specifically in the (xy) polarization configuration, we observed three well resolved peaks with Raman shifts 231 cm^{-1}, 249 cm^{-1}, 258 cm^{-1} around where the highly prominent peak in the unpolarized spectrum was observed. Although not clearly resolved in the unpolarized spectrum due to its low intensity and proximity to the strong peak at 259 cm^{-1}, the signature of the peak at 231 cm^{-1} is still visible. As seen in the (xy) polarization spectrum, this peak is broad, characteristic of a peak due to a second-order Raman mode. Its low intensity also supports our argument that this peak is due to a second-order Raman mode. The peak at 249 cm^{-1} as earlier stated has been assigned as an $E_{2g}^{(1)}$ mode. This we arrived at by considering that a typical E_g mode which is doubly degenerate appears in both the (xx) and (xy) polarization spectra. This mode is better resolved in the (xy) polarization spectrum, because in this spectrum the A_{1g} mode is greatly suppressed. The peak at 258 cm^{-1} is assigned as an A_{1g} mode. The presence of this mode, which according to selection rules is supposed to be absent in the (xy) configuration, has been attributed to depolarization whose origin is from crystal surface imperfections [41]. To support the assignment of this peak to the A_{1g} mode, we observe that its intensity in the (xy) polarization configuration is about one-third of its value in the (xx) polarization configuration.

Apart from the two first-order Raman modes observed, there appeared two second-order Raman modes in our spectra of 2H-WSe_2. As expected for second-order Raman

modes [69], these modes were polarization independent. We observed at least two new second-order modes at 221 cm^{-1} and 231 cm^{-1} which have not been reported in the literature. We attribute the presence of peaks due to these modes in our spectra to the 830 nm laser source we used. It has been observed by Sourisseau *et al.* [69] while studying second order Raman effect in 2H-WS_2 that the appearance and intensities of multi-phonon bands in this material is laser energy dependent. It was observed that by simply changing the laser excitation from 530.9 nm to 676.4 nm, more second-order Raman modes appeared in the Raman spectra of 2H-WS_2. Because 2H-WSe_2 and 2H-WS_2 share the same structure, a similar effect might be expected, which might explains why more second-order Raman modes are observed than previously reported by other authors. Assigning these modes requires an in-depth knowledge of the phonon dispersion curve, and thus only their presence are reported here.

It is imperative to see how results of previous Raman scattering studies of WSe_2 compares to results from the present work. In the work reported by Zhao *et al.* [24], two prominent peaks and five multi-phonon bands were observed. They concluded that the peak at 248 cm^{-1} in their polarization studies to be due to the $E^{(1)}_{2g}$ mode, while a peak was observed at 250 cm^{-1} and was assigned as the A_{1g} mode. The Raman shift of the former is within $\simeq$ 1 cm^{-1} of the corresponding peak in our spectra a wavenumber equal to our observer shift. The latter is about 9 cm^{-1} less our observed shift. The authors reference [24] observed a peak at $\simeq$ 260 cm^{-1} but assigned it as due to a second order Raman mode instead. We suspect an error in their A_{1g} mode assignment in this regard. It is noteworthy that a 633 nm excitation was used in their study which might also explain why their results are different from ours. Table 4.6 shows how the multi-phonon bands frequency of Zhao *et al.* compares

with those of the present work.

Mead *et al.* [41] observed a near degeneracy of two peaks at 252 cm^{-1} in a 90 degree scattering geometry using a 488 nm and 514.5 nm laser excitation. The peak at 250 cm^{-1} was assigned as the $E_{2g}^{(1)}$ mode while that at 253 cm^{-1} was assigned as the A_{1g} mode. The fact that they reported a near degeneracy at 252 cm^{-1} is inconsistent with our findings where we found the $E_{2g}^{(1)}$ mode at 249 cm^{-1} and the A_{1g} mode at 258 cm^{-1}. Likewise their mode intensities do not match ours, it is noteworthy that this is probably due to the conditions under which their spectra was collected. One possible difference was the collection of their spectra at a temperature of 80 K. We can not say for certain why this might be a source of inconsistency. It would be contrary to reports that a decrease in temperature brings about a blue shift in Raman modes [71, 72].

Sahin *et al.* [33] reported that in bulk samples of 2H-WSe_2, the $E_{2g}^{(1)}$ mode and A_{1g} mode are degenerate. Their result is inconsistent with our observation, and also the Raman shift is different from that obtained in the present work. They reported the Raman shift of the prominent peak as 252.2 cm^{-1}, which then splits to two peaks as thickness decreased, one at 250 cm^{-1} and the other at 261 cm^{-1}. The accuracy of this result can be questioned owing to the fact that no detailed polarization studies were given in their report, only theoretical calculations. The laser excitation wavelength used for the study was also not stated. Surprisingly, Mead *et al.*, and Sahin *et al.* did not make mention of any observation of second-order Raman modes.

Hai Li *et al.* [70] found for single crystals of 2H-WSe_2 that the $E_{2g}^{(1)}$ and A_{1g} modes occurring at 247 cm^{-1} and 257 cm^{-1} respectively, are not degenerate. They also reported similar intensity for both modes. These two modes are separated by

about 10 cm^{-1} which is consistent with our findings and their argument that these modes are not degenerate is consistent with results presented here. They also stated that by simply increasing the laser beam power, more featured Raman peaks were observed. The Raman shift reported for these modes and some of the second-order Raman modes reported are 2 cm^{-1} to 3 cm^{-1} different from the values reported here. This might be due to some calibration error in their Raman equipment as no mention of the equipment calibration was mentioned in the paper, but in our case we used the 521 cm^{-1} line of silicon as calibration before collecting the spectra reported here.

4.3 Brillouin Scattering Studies of WSe_2

Brillouin spectra collected from single crystals of 2H-WSe_2 are presented in Figure 4.13. The frequency shift (in GHz) is shown on the horizontal axis while the vertical axis shows scattered light intensity (in arbitrary units). The numbers on the right hand side of the spectrum indicate the value of the incident angle.

In the spectra shown in Figure 4.13, a sharp peak labelled R has been identified. This happens to be the only peak observed in the Brillouin spectrum of WSe_2. The low frequency shift (<5 GHz) at which R appeared necessitated our choice of a small Free Spectral Range − 20 GHz (mirror spacing of 7.50 mm) for all spectra collected. This was necessary so as to bring the peak further out of the cut-off region of the shutter. This explains why the peak R is better resolved at higher angles of incidence than at lower incident angles where the peak is in the region of the spectrum cut-off by a shutter in the Brillouin experiment set-up. It is obvious from the spectra that the frequency shift at which this peak appears is dependent on the angle of incidence

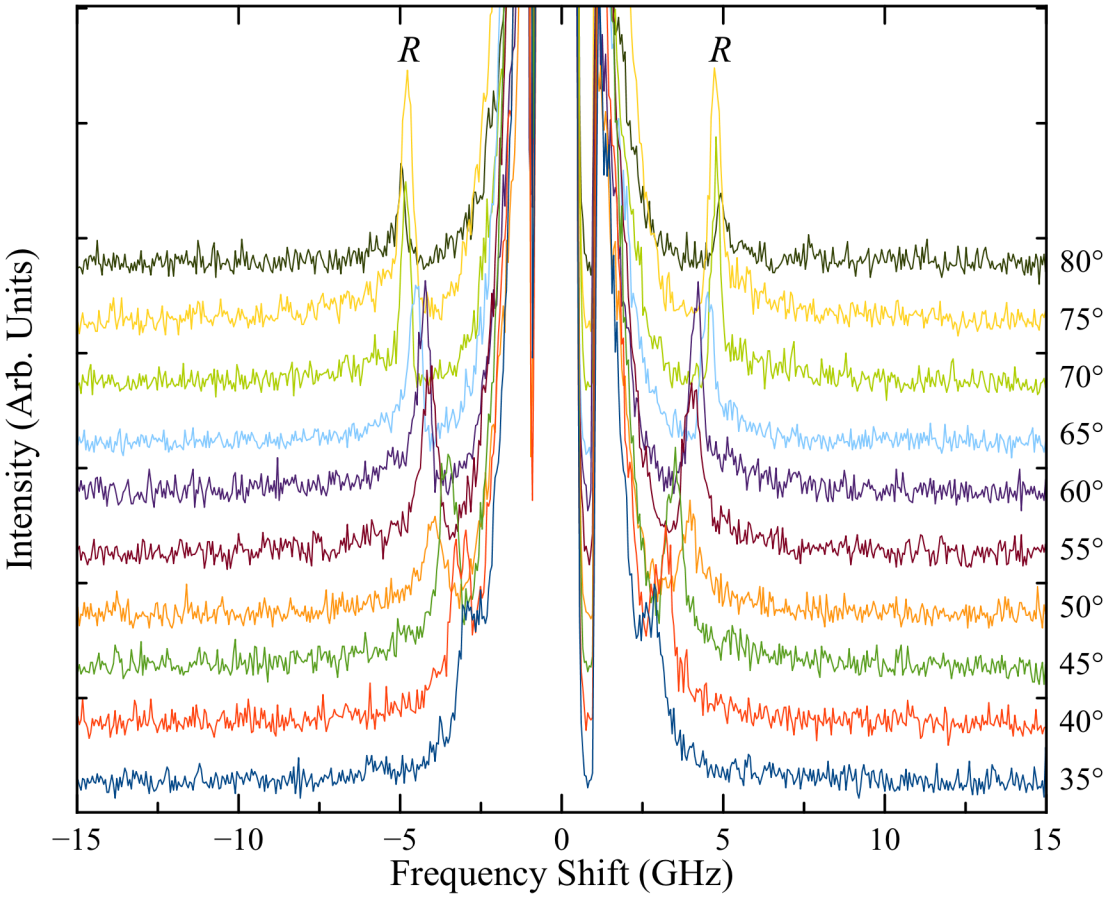

Figure 4.13: Brillouin spectra of WSe_2 for different angles of incidence.

measured from the normal to the sample surface.

Table 4.7 shows the angle of incidence, the corresponding anti-Stokes and Stokes frequency shifts, and the average of both frequency shifts. The last two columns of Table 4.7 shows the width of the observed peak for each angle of incidence. From the Table, it appears that the relationship between average frequency and the angle of incidence is linear. A linear fit of Equation (2.9) to the data in Table 4.7 for average frequency shift versus sin θ is shown in Figure 4.14. As a result of the high quality of the fit, we assign the R peak to the Rayleigh surface mode. We note that, as

seen from Equation (2.9), the Rayleigh surface mode (whose peak exhibits a strong intensity for opaque materials) has its frequency shift directly proportional to the sine of the angle of incidence. This trend we observed in the plot of frequency shift versus the sine of the angle of incidence measured from a normal to the sample surface. We should also mention that our sample is opaque. Thus supporting our initial argument that this peak is indeed due to the Rayleigh surface mode. The Rayleigh surface wave velocity was extracted from the slope of the graph and was found to be 1338 $\pm$ 20 m/s.

From Table 4.7, a decrease in peak width with an increase in the angle of incidence has been observed. We are unable to tell how significant this trend at present.

Table 4.7: Angle of incidence as a function of frequency of Rayleigh surface mode

θ ($\pm$ 1°)	Anti-Stokes Shift ($\pm$ 0.05 GHz)	Stokes Shift ($\pm$ 0.05 GHz)	Average Shift ($\pm$ 0.1 GHz)	Anti-Stokes Width (FWHM) ($\pm$ 0.1 GHz)	Stokes Width (FWHM) ($\pm$ 0.1 GHz)
35	2.98	2.79	2.9	0.5	0.6
40	3.17	3.14	3.2	0.4	0.4
45	3.60	3.47	3.5	0.3	0.3
50	4.06	3.93	4.0	0.3	0.3
55	4.20	4.06	4.1	0.3	0.3
60	4.37	4.14	4.3	0.2	0.2
65	4.64	4.52	4.6	0.2	0.2
70	4.92	4.76	4.8	0.2	0.2
75	4.89	4.74	4.8	0.2	0.2
80	5.05	4.92	5.0	0.1	0.1

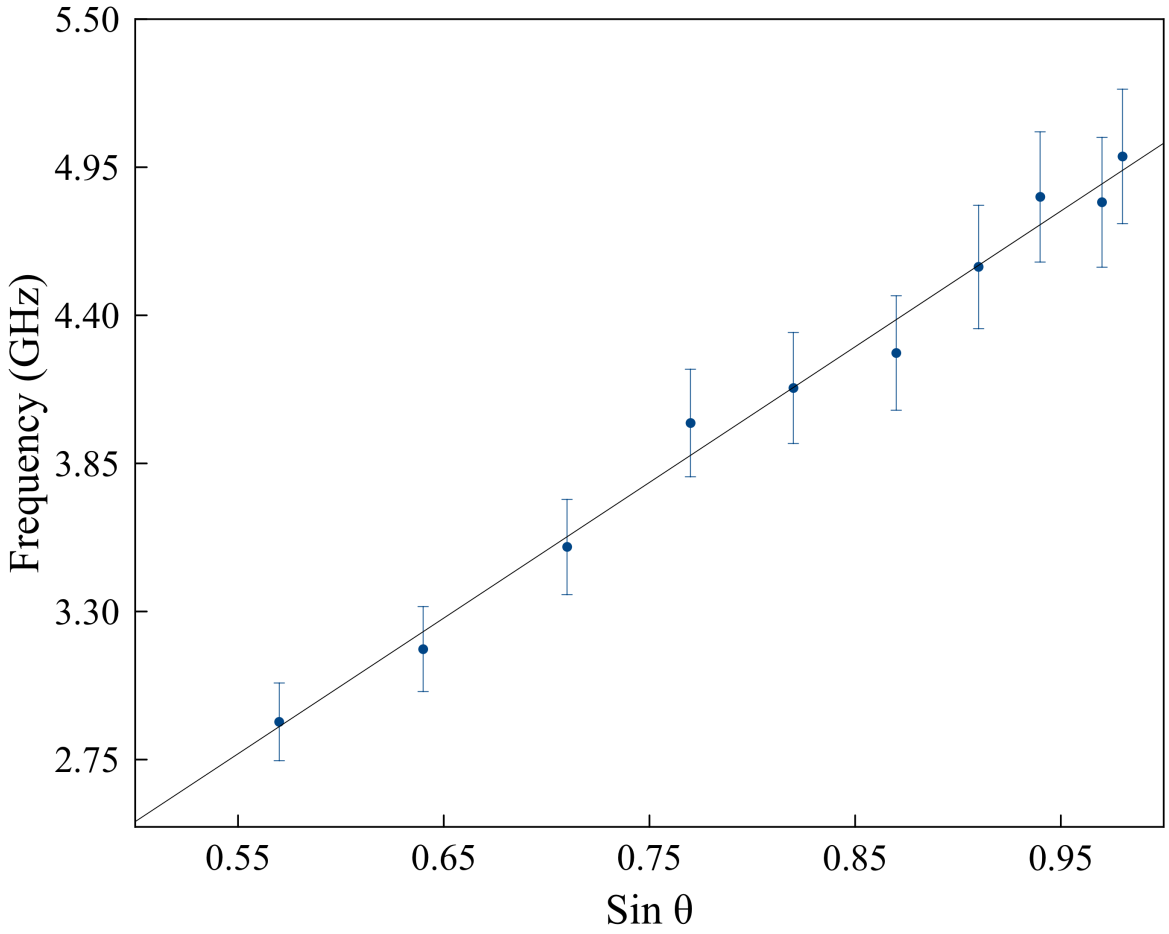

Figure 4.14: Frequency shift of R peak vs Sin θ.

4.3.1 Discussion

The observed peak R indeed exhibits all the properties of a Rayleigh surface mode viz: the material is opaque which explains why the peak is strong, it is a sharp peak, it appears at a low frequency shift with a linear relationship between the frequency shift and the sine of the angle of incidence. Although bulk modes are expected to be present

in this material, they were not observed in this experiment. This is most probably due to the fact that scattering due to elasto-optic mechanism is precluded due to sample opacity therefore only surface ripple mechanism contributes appreciably. Increasing the Laser power might fix this, but could also result in sample damage.

We compared our results of the Rayleigh surface mode velocity with those reported for some other Transition metal dichalcogenides in Table 4.8. The table shows our results for 2H-WSe_2 and those reported by Harley and Fleury [46] on Brillouin Scattering studies on 2H$-TaSe_2$ and 2H$-NbSe_2$ obtained at room temperature in a backscattering geometry. From the Table, we see a that their velocities are similar to our result for 2H-WSe_2.

Harley and Fleury [46] employed similar conditions as we did in identifying the Rayleigh surface mode. A sharp low-frequency peak, whose frequency was proportional to the angle of incidence was observed in their spectrum. They observed a weak bulk mode whose velocity was $\simeq 5000$ m/s in both materials. We should mention that Harley and Fleury [46] reported using incident beam power ranging between 50 mW and 200 mW. This evidence supports the reason why we did not observe bulk modes in our Brillouin scattering studies of 2H-WSe_2 because our beam power was 60 mW so as to avoid damaging the sample.

Table 4.8: Rayleigh surface wave in transition metal dichalcogenide from Brillouin scattering experiment.

	Sample	Rayleigh Surface Velocity (m s^{-1})
This Work	2H−WSe_2	1338 ± 20
[46]	2H−$TaSe_2$	1220 ± 10
[46]	2H−$NbSe_2$	1571 ± 10

Chapter 5

Conclusions

Brillouin light scattering and Raman scattering have been employed to study the phonon dynamics in Bi_2Se_3, Bi_2Te_3, Sb_2Te_3 and WSe_2. Information about the electronic and vibrational properties of these materials were extracted from the resulting experimental spectra. Our results and discussion is intended to defuse all existing arguments about the vibrational properties of these materials. The main results of this thesis are as follows:

First, the vibrational properties of bulk samples of Bi_2Se_3, Bi_2Te_3, and Sb_2Te_3 were studied using Raman spectroscopy technique. Two of the four Raman active modes were observed and assigned accordingly after carrying out polarization studies. The Raman shift of the observed vibrational modes has been reported. It was also observed that the shift and intensity of the observed peaks are independent of thickness of bulk samples. From our observations, we deduced that the choice of laser excitation could induce resonance effects in crystal thereby enhancing the intensity of peaks corresponding to some vibrational modes.

Second, Raman scattering studies of WSe_2 revealed a combination of first-order and second-order Raman modes. A prominent peak at 259 cm^{-1} in the Raman spectrum of WSe_2 was determined to be polarization dependent. Polarization studies revealed the peak splitting into three other peaks. The peaks with relatively low intensities that appeared in the spectrum were attributed to multi-phonon processes that give rise to second-order Raman modes. Two of the observed second-order peaks observed in this study have not been reported in literature before. We have yet to assign the peaks to particular vibrational modes, but report their presence here. We attributed their presence to our choice of laser excitation wavelength which tends to excite more phonons. This scenario has been observed in materials with similar structure to WSe_2 [69].

Last, the velocity of Rayleigh surface wave of 2H-WSe_2 was determined from Brillouin light scattering experiment. The only peak that appeared in the spectrum was identified as due to Rayleigh surface mode owing to its dependence on the angle of incidence. A plot of frequency vs $\sin\theta$ (where θ is the angle of incidence) was found to be linear. The velocity of the Rayleigh surface wave was extracted from the slope of the graph. Its value was compared to those previously reported for other members of the transition metal dichalcogenide family, namely $TaSe_2$ and $NbSe_2$.

Although a direct connection has not been made between the topological insulating property of Bi_2Se_3, Bi_2Te_3, and Sb_2Te_3 and their vibrational properties, this thesis provides a quantitative and robust discussion on the vibrational properties of these materials as well as those of WSe_2 which was initially absent in reported literature.

This thesis reports new results of the vibrational properties of Bi_2Se_3, Bi_2Te_3, Sb_2Te_3 and WSe_2. The results of this work also addressed the confusions surrounding

the vibrational properties of these materials reported in previous work.

Bibliography

[1] M. König, S. Wiedmann, C. Brüne, A. Roth, H. Buhmann, L. W. Molenkamp, X. Qi, and S. Zhang. Science **318**, 766 (2007).

[2] P. Gehring, H. M. Benia, Y. Weng, R. Dinnebier, C. R. Ast, M. Burghard, and K. Kern. Nano Lett. **13**, 1179 (2013).

[3] C. L. Kane and E. J. Mele. Phys. Rev. Lett. **95**, 226801 (2005).

[4] C. L. Kane and E. J. Mele. Phys. Rev. Lett. **95**, 146802 (2005).

[5] F. Liang and C. L. Kane. Phys. Rev. B **76**, 045302 (2007).

[6] J. E. Moore and L. Balents. Phys. Rev. B **75**, 121306 (2007).

[7] R. Roy. Phys. Rev. B **79**, 195322 (2009).

[8] B. A. Bernevig, T. L. Hughes, and S. Zhang. Science **314**, 1757 (2006).

[9] D. Hsieh, D. Qian, L. Wray, Y. Xia, Y. S. Hor, R. J. Cava, and M. Z. Hasan. Nature **452**, 970 (2008).

[10] Y. Xia, D. Qian, D. Hsieh, R. Shankar, H. Lin, A. Bansil, A. V. Fedorov, D. Grauer, Y. S. Hor, R. J. Cava, and M. Z. Hasan. arXiv:0907.3089v1 (2009).

[11] H. Zhang, C. Liu, X. Qi, X. Dai, Z. Fang, and S. Zhang. Nat. Phys. **5**, 438 (2009).

[12] M. Z. Hasan and C. L. Kane. Rev. Mod. Phys. **82**, 3045 (2010).

[13] B. Bernevig and T. Hughes. *Topological Insulators and Topological Superconductors* (Princeton University Press, 2013).

[14] D. Hsieh, Y. Xia, D. Qian, L. Wray, F. Meier, J. H. Dil, J. Osterwalder, L. Patthey, A. V. Fedorov, H. Lin, A. Bansil, D. Grauer, Y. S. Hor, R. J. Cava, and M. Z. Hasan. Phys. Rev. Lett. **103**, 146401 (2009).

[15] P. Cheng, C. Song, T. Zhang, Y. Zhang, Y. Wang, J. Jia, J. Wang, Y. Wang, B. Zhu, X. Chen, X. Ma, K. He, L. Wang, X. Dai, Z. Fang, X. Xie, X. Qi, C. Liu, S. Zhang, and Q. Xue. Phys. Rev. Lett. **105**, 076801 (2010).

[16] S. Urazhdin, D. Bilc, S. D. Mahanti, S. H. Tessmer, T. Kyratsi, and M. G. Kanatzidis. Phys. Rev. B **69**, 085313 (2004).

[17] J. O. Jenkins, J. A. Rayne, and R. W. Ure. Phys. Rev. B **5**, 3171 (1972).

[18] K. M. F. Shahil, M. Z. Hossain, D. Teweldebrhan, and A. Balandin. Appl. Phys. Lett. **96**, 153103 (2010).

[19] K. M. F. Shahil, M. Z. Hossain, V. Goyal, and A. A. Balandin. J. Appl. Phys. **111**, 054305 (2012).

[20] G. Sosso, R. Mazzarello, S. Caravati, M. Parrinello, and M. Bernasconi (2010).

[21] W. Richter, H. Kohler, and C. R. Becker. Phys. Stat. Sol. B **84**, 619 (1977).

[22] V. Russo, A. Bailini, M. Zamboni, M. Passoni, C. Conti, C. S. Casari, B. A. Li, and C. E. Bottani. J. Raman Spectrosc. **39**, 205 (2008).

[23] L. M. Goncalves, C. Couto, P. Alpuim, A. G. Rolo, F. Völklein, and J. H. Correia. Thin Solid Films **518**, 2816 (2010).

[24] W. Zhao, Z. Ghorannevis, K. K. Amara, J. R. Pang, M. Toh, X. Zhang, C. Kloc, P. H. Tan, and G. Eda. Nanoscale **5**, 9677 (2013).

[25] J. Zhang, Z. Peng, A. Soni, Y. Zhao, Y. Xiong, B. Peng, J. Wang, M. S. Dresselhaus, and Q. Xiong. Nano Lett. **11**, 2407 (2011).

[26] X. Chen, H. D. Zhou, A. Kiswandhi, I. Miotkowski, Y. P. Chen, P. A. Sharma, A. L. Lima Sharma, M. A. Hekmaty, D. Smirnov, and Z. Jiang. Appl. Phys. Lett. **99**, 261912 (2011).

[27] X. Qi and S. Zhang. Rev. Mod. Phys. **83**, 1057 (2011).

[28] D. Teweldebrhan, V. Goyal, and A. A. Balandin. arXiv:1003.1398v1 (2010).

[29] D. Teweldebrhan, V. Goyal, and A. A. Balandin. Nano Lett. **10**, 1209 (2010).

[30] L. Fu, C. L. Kane, and E. J. Mele. Phys. Rev. Lett. **98**, 106803 (2007).

[31] A. K. Geim and K. S. Novoselov. Nat. Mater. **6**, 183 (2007).

[32] K. S. Novoselov, S. V. Morozov, T. M. G. Mohinddin, L. A. Ponomarenko, D. C. Elias, R. Yang, I. I. Barbolina, P. Blake, T. J. Booth, D. Jiang, J. Giesbers, E. W. Hill, and A. K. Geim. Phys. Stat. Sol. B **244**, 4106 (2007).

[33] H. Sahin, S. Tongay, S. Horzum, W. Fan, J. Zhou, J. Li, J. Wu, and F. M. Peeters. Phys. Rev. B **87**, 165409 (2013).

[34] D. Xiao, G.-B. Liu, W. Feng, X. Xu, and W. Yao. Phys. Rev. Lett. **108**, 196802 (2012).

[35] C. Isaac, T. Jifa, M. Ireneusz, and C. Yong. arXiv:1209.2919 (2012).

[36] Y. Kim, X. Chen, Z. Wang, J. Shi, I. Miotkowski, Y. P. Chen, P. A. Sharma, A. L. Lima Sharma, M. A. Hekmaty, Z. Jiang, and D. Smirnov. Appl. Phys. Lett. **100**, 071907 (2012).

[37] I. Bushra, S. Satyaprakash, P. S. G. Anand, A. Majid, J.-F. G. Maxime, S. K. Ram, and C. Ratnamala. arXiv:1401.4346 (2014).

[38] V. Goyal, D. Teweldebrhan, and A. A. Balandin. Appl. Phys. Lett. **97**, 133117 (2010).

[39] G. C. Sosso, S. Caravati, and M. Bernasconi. J. Phys.: Condens. Matter **21**, 095410 (2009).

[40] W. Cheng and S. Ren. Phys. Rev. B **83**, 094301 (2011).

[41] D. G. Mead and J. C. Irwin. Can. J. Phys. **55**, 379 (1977).

[42] P. Tonndorf, R. Schmidt, P. Böttger, X. Zhang, J. Börner, A. Liebig, M. Albrecht, C. Kloc, O. Gordan, D. R. T. Zahn, S. M. de Vasconcellos, and R. Bratschitsch. Opt. Express **21**, 4908 (2013).

[43] W. Zhao, Z. Ghorannevis, L. Chu, M. Toh, C. Kloc, P. Tan, and G. Eda. ACS Nano **7**, 791 (2013).

[44] H. Wang, D. Kong, P. Johanes, J. J. Cha, G. Zheng, K. Yan, N. Liu, and Y. Cui. Nano Lett. **13**, 3426 (2013).

[45] L. Feng, N. Li, M. Yang, and Z. Liu. Materials Research Bulletin **50**, 503 (2014).

[46] R. T. Harley and P. A. Fleury. J. Phys. C: Solid State Phys. **12**, L863 (1979).

[47] M. Born and K. Huang. *Dynamical theory of crystal lattices*. International series of monographs on physics (Clarendon Press, 1954).

[48] A. M. Marvin, V. Bortolani, and F. Nizzoli. J. Phys. C: Solid State Phys. **13**, 299 (1980).

[49] L. R. Adv. Phys. **13**, 423 (1964).

[50] P. Bruesch. *Phonons: Theory and Experiments II* (Springer, 1986).

[51] G. Burns and A. M. Glazer. *Space groups for solid state scientists*, (Academic Press, New York1978).

[52] T. Hahn. *International Tables for Crystallography, Space-Group Symmetry* (Wiley, 2005).

[53] M. Tinkham and G. McKay. *Group theory and Quantum Mechanics*, (Dover Publications, Inc., Mineola, New York1992), second edn.

[54] S. Bhagavantam and T. Venkatarayudu. *Theory of Groups and its Applications to Physical Problems* (Academic Press, INC., 1969), second edn.

[55] A. D. Bernardo, R. E. N., and W. B. W. American Mineralogist **57**, 255 (1972).

[56] W. G. Dawson and D. W. Bullet. J. Phys. C: Solid State Phys. **20**, 6159 (1987).

[57] R. Wyckoff. *Crystal Structures* (Wiley, 1969).

[58] Y. L. Chen, J.-H. Chu, J. G. Analytis, Z. K. Liu, K. Igarashi, H.-H. Kuo, X. L. Qi, S. K. Mo, R. G. Moore, D. H. Lu, M. Hashimoto, T. Sasagawa, S. C. Zhang, I. R. Fisher, Z. Hussain, and Z. X. Shen. Science **329**, 659 (2010).

[59] W. V. University. Standard operating procedure: Renishaw invia raman spectrometer.

[60] M. Vaughan. *The Fabry-Perot Interferometer: History, Theory, Practice and Applications*. Series in Optics and Optoelectronics (Taylor & Francis, 1989).

[61] P. Hariharan. *Basics of Interferometry* (Elsevier Science, 2010).

[62] J. R. Sandercock. *Tandem Fabry-Perot Interferometer TFP-1*. JRS Scientific Instruments, 8932 Mettmenstetten, Switzerland.

[63] J. R. Sandercock. *GHOST 6.60 Multichannel Analyser*. JRS Scientific Instruments, Fabrik am Weiher, 8909 Zwillikon-Switzerland.

[64] C. Wang, X. Zhu, L. Nilsson, J. Wen, G. Wang, X. Shan, Q. Zhang, S. Zhang, J. Jia, and Q. Xue. Nano Research **6**, 688 (2013).

[65] P. Nemec, V. Nazabal, A. Moreac, J. Gutwirth, L. Benes, and M. Frumar. Materials Chemistry and Physics **136**, 935 (2012).

[66] N. Abrikosov. *Semiconducting II-IV, IV-VI, and V-VI Compounds* (Plenum Press, 1969).

[67] S. Murugkar, R. Merlin, A. Botchkarev, A. Salvador, and H. Morkoc. J. Appl. Phys. **77**, 6042 (1995).

[68] I. S. Gorban' and V. I. Lugovoi. J. Appl. Spectrosc. **24**, 233 (1976).

[69] C. Sourisseau, F. Cruege, M. Fouassier, and M. Alba. Chem. Phys. **150**, 281 (1991).

[70] H. Li, G. Lu, Y. Wang, Z. Yin, C. Cong, Q. He, L. Wang, F. Ding, T. Yu, and H. Zhang. Small **9**, 1974 (2013).

[71] M. Deshpande, S. V. Bhatt, V. Sathe, R. Rao, and S. Chaki. Physica B: Condensed Matter **433**, 72 (2014).

[72] S. Xie, E. Iglesia, and A. T. Bell. J. Phys. Chem. B **105**, 5144 (2001).